Click Here for Full Article

Retrieval of phytoplankton biomass from simultaneous inversion of reflectance, the diffuse attenuation coefficient, and Sun-induced fluorescence in coastal waters

Yannick Huot,[1] Catherine A. Brown,[1] and John J. Cullen[2]

[1]   A model has been developed to retrieve phytoplankton absorption, a proxy for phytoplankton biomass, from observations of reflectance (R) and the diffuse attenuation coefficient (K_d) collected by moored radiometers in coastal waters, where high concentrations of chromophoric dissolved organic matter (CDOM) confound conventional ocean color algorithms. The inversion uses simultaneously two forward models: (1) a look-up table (LUT) that accounts for instrument geometry and the effect of the solar angle on both R and K_d and (2) an analytical function describing the effects of Sun-induced fluorescence (SIF) of chlorophyll on R. Estimates of phytoplankton biomass (mostly from SIF), the absorption by colored matter, and the particulate backscattering coefficients (mostly from the LUT) are obtained by optimizing the amplitude and shape of the absorption and backscattering coefficients in the forward model to best match the observations. An equation describing the quantum yield of fluorescence (photons fluoresced/photons absorbed) as a function of incident irradiance constrains the model and allows estimates of phytoplankton absorption. Innovations include: the utilization of both R and K_d, providing good separation of the effects of backscattering from absorption; avoidance of reflectance bands between 400 and 600 nm, thereby avoiding interference from bottom reflection and CDOM fluorescence; utilization of the full emission band of SIF; and accounting for the irradiance-dependence of its quantum yield. The model effectively retrieved chlorophyll concentration from an independent data set — $r = 0.76$, n = 93, with a mean absolute percent error (MAPE) of 24%; this is better than a modern ocean color algorithm (OC4V4) on its validation data set, when restricted to the same range of chlorophyll ($r = 0.67$, n = 384, MAPE = 51%).

1. Introduction

[2]   When it was recognized that variations in the concentrations of colored dissolved and particulate matter were causing the ocean's hues [see *Yentsch*, 1960, and references therein], the challenge became to estimate these concentrations from measurements of ocean color and other properties of the light field. This is the so-called inverse problem of ocean optics [*Gordon*, 2002]: retrieving the inherent optical properties (IOPs, which are determined solely by the water constituents) from apparent optical properties (AOPs, which depend on both the IOPs and the light field [*Preisendorfer*, 1976]), and inferring from the IOPs the constituents of the water. The apparent optical properties that are measured and analyzed include the diffuse attenuation coefficient, which describes the rate of loss of irradiance with depth, and spectral reflectance, which is the ratio of upwelling radiance to downwelling irradiance. The IOPs retrieved with modern algorithms include the scattering or backscattering coefficients and absorption coefficients [*Carder et al.*, 1999; *Garver and Siegel*, 1997; *Loisel and Morel*, 1998; *Loisel and Stramski*, 2000; *Maritorena et al.*, 2002; *Roesler and Perry*, 1995; *Roesler*, 2003]. The concentrations of the constituents can be obtained because chromophoric dissolved and particulate matter influence the spectral radiance field through their concentrations and mass specific IOPs. In general, the impetus has been to estimate the concentration and nature of two classes of constituents that provide insight into biogeochemical oceanic processes: chromophoric dissolved organic matter (CDOM [*Fichot and Miller*, 2002; *Johannessen et al.*, 2003; *Siegel et al.*, 2002]), and the pigments of phytoplankton, particularly chlorophyll as an indicator of biomass [*O'Reilly et al.*, 1998; *Siegel et al.*, 2002].

[1]Laboratoire d'Océanographie de Villefranche, Villefranche-sur-mer, France.
[2]Department of Oceanography, Dalhousie University, Halifax, Nova Scotia, Canada.

[3] Ocean color is determined by the absorption and scattering of sunlight in the surface layer. There are two types of scattering. Elastic scattering affects only the direction of a photon, whereas inelastic scattering produces photon at a different wavelength than the incident photon, which can also augment the upwelling light field [*Bukata et al.*, 2004; *Mobley*, 1994; *Pozdnyakov and Grassl*, 2003]. Inelastic processes that have a significant effect in the ocean include Raman scattering by water [*Marshall and Smith*, 1990; *Sathyendranath and Platt*, 1998], and fluorescence by CDOM [e.g., *Hawes*, 1992; *Vodacek et al.*, 1997] and some algal pigments (mostly the chlorophylls and phycobiliproteins [*Gordon*, 1979; *Hoge et al.*, 2003]) including their decomposition products [*Fuchs et al.*, 2002; *Yentsch and Menzel*, 1963]. Inelastic processes can be included explicitly or implicitly in inverse models.

[4] In this contribution, we develop an inverse model that accounts for the effects of elastic processes on reflectance and the diffuse attenuation coefficient as well as for the effect of Sun-induced chlorophyll fluorescence on reflectance. The inversion is based on optimizing the contributions from various IOPs [e.g., *Garver and Siegel*, 1997; *Maritorena et al.*, 2002; *Roesler and Perry*, 1995] in a spectral forward model of AOPs to retrieve nonalgal colored matter absorption and particulate backscattering. We apply the model to data from optical moorings in Lunenburg Bay, a coastal embayment in Nova Scotia, Canada. In the blue wavebands, the waters of the bay are characterized by a dominant contribution to absorption from CDOM, thereby preventing the retrieval of phytoplankton biomass using absorption-based models. We therefore utilize the Sun-induced chlorophyll fluorescence signature to infer phytoplankton absorption. To achieve this, the model is built in two parts, one for the elastically scattered photons, generally consistent with several other inverse models (but including several necessary modifications), and one for photons fluoresced by chlorophyll *a*, which includes a function accounting for the irradiance-dependence of the quantum yield due to competition with heat dissipation (nonphotochemical quenching).

[5] The method we present is general and allows for the inversion of simultaneous measurements of different AOPs. For the validation of this approach, we apply it to the retrieval of phytoplankton biomass using a hyperspectral Tethered Spectral Radiometer Buoy (TSRB, Satlantic Inc.) and a K-chain (a series of downwelling irradiance sensors at fixed depths, TACCS, Satlantic Inc.) deployed in Lunenburg Bay. The TSRB has a downwelling irradiance sensor above the surface and an upwelling radiance sensor at 0.65 m below the surface, requiring special methods to calculate reflectance. The main objective behind the development of these methods was the retrieval of phytoplankton biomass for utilization in an assimilative model of the Lunenburg Bay ecosystem.

2. Background

2.1. Contributions to Upwelling Radiance and Reflectance

[6] Ignoring fluorescence by phycobiliproteins and phaeopigments and nonsolar sources such as bioluminescence, the upwelling radiance ($L_u(\lambda, z)$, μmol m^{-2} s^{-1} nm^{-1} sr^{-1}, see Table 1 for the notation) at depth z (m) and wavelength λ (nm) in the surface waters of the ocean can be separated into contributions from five sources as

$$L_u(\lambda, z) = L_{ub}(\lambda, z) + L_{uR}(\lambda, z) + L_{uf}(\lambda, z) \\ + L_{uCDOM}(\lambda, z) + L_{ubottom}(\lambda, z), \quad (1)$$

where the terms on the right represent upwelling radiance originating from elastic scattering, $L_{ub}(\lambda, z)$, Raman scattering, $L_{uR}(\lambda, z)$, chlorophyll *a* fluorescence, $L_{uf}(\lambda, z)$, CDOM fluorescence, $L_{uCDOM}(\lambda, z)$, and bottom reflection, $L_{ubottom}(\lambda, z)$. In this equation, a photon is associated with the last scattering or fluorescence event that occurs before it travels upwards through the plane at depth z.

[7] For measurements from floating radiometers, where the downwelling irradiance sensor is above the surface and the radiance sensor is positioned at depth z_{Lu} (m), it is convenient to define sea surface reflectance ($R_L(\lambda)$, sr^{-1}) as the ratio of upwelling radiance at a depth z_{Lu} below the surface to downwelling planar irradiance above the surface $E_d(\lambda, 0^+)$ (μmol m^{-2} s^{-1} nm^{-1}) leading to

$$R_L(\lambda) = \frac{L_{ub}(\lambda, z_{Lu})}{E_d(\lambda, 0^+)} + \frac{L_{uR}(\lambda, z_{Lu})}{E_d(\lambda, 0^+)} + \frac{L_{uf}(\lambda, z_{Lu})}{E_d(\lambda, 0^+)} \\ + \frac{L_{uCDOM}(\lambda, z_{Lu})}{E_d(\lambda, 0^+)} + \frac{L_{ubottom}(\lambda, z_{Lu})}{E_d(\lambda, 0^+)} \\ = R_{Lb}(\lambda, z_{Lu}) + R_{LR}(\lambda, z_{Lu}) + R_{Lf}(\lambda, z_{Lu}) \\ + R_{LCDOM}(\lambda, z_{Lu}) + R_{Lbottom}(\lambda, z_{Lu}). \quad (2)$$

[8] The subscripts for $R_L(\lambda)$ are the same as in equation (1). Note that this additive representation of an AOP is only valid for the single scattering approximation or if we consider only the last photon source; it is used here to guide the discussion and development of our model.

2.2. Inverse Models Using Spectral Shapes for the Inherent Optical Properties

[9] We are using an inversion method that optimizes a forward model that describes the AOPs by varying the spectral shapes and amplitudes of the IOPs to match the measured spectral light field [*Roesler and Perry*, 1995]. This type of inversion requires the description of an AOP in terms of IOPs, which is usually in the form of an analytical function (the so-called explicit inversions [e.g., *Gordon*, 2002]).

[10] Many models exist [e.g., *Albert and Mobley*, 2003; *Gordon et al.*, 1988; *Morel*, 1988; *Morel and Loisel*, 1998; *Morel et al.*, 2002] that express reflectance due to elastic scattering as a function of IOPs. They are usually of the form,

$$R_{Lb}(\lambda) = f(b_b(\lambda), a(\lambda)), \quad (3)$$

where $f()$ represents some function of $b_b(\lambda)$ (m^{-1}), the total backscattering coefficient, and $a(\lambda)$ (m^{-1}), the total absorption coefficient. The total backscattering coefficient can be expressed as the sum of particulate backscattering ($b_{bpart}(\lambda)$, m^{-1}) and water backscattering ($b_{bw}(\lambda)$, m^{-1}): $b_b(\lambda) = b_{bpart}(\lambda) + b_{bw}(\lambda)$. The total absorption coefficient can be separated into contributions from CDOM ($a_{CDOM}(\lambda)$, m^{-1}), nonalgal particulate matter ($a_{NAP}(\lambda)$, m^{-1}), phyto-

Table 1. List of Symbols and Units

Symbol	Description
a a_{CM} a_ϕ a_w a_{nw} a_{CDOM} a_{NAP}	Total, colored matter, phytoplankton, water, nonwater, CDOM, and nonalgal particulate absorption coefficients, m^{-1}
$\bar{a}_\phi^{490}(\lambda)$ $\bar{a}_{CM}^{400}(\lambda)$	Mean phytoplankton and colored matter absorption spectra for the summer of 2003 in Lunenburg Bay normalized to 490 and 400 nm respectively, Unitless
a_ϕ^{yield}	Phytoplankton absorption coefficient obtained from the inverse model when the quantum yield of fluorescence is held constant. Used as the irradiance dependence of φ_f, m^{-1}
a_f	Attenuation coefficient for upwelling fluoresced radiance, m^{-1}
b_b b_{bpart} b_{bw} b_{bnw}	Total, particulate, water, and nonwater backscattering coefficients, m^{-1}
ϕ_{ai} ϕ_{bi}	ith observation of spectral components for absorption and backscattering, Units vary
E_d $\overset{o}{E}$ E_d^{clear}	Measured downwelling planar and scalar irradiance and modeled planar irradiance, $\mu mol\ m^{-2}\ s^{-1}\ nm^{-1}$
E_{PUR}^{490}	Scalar irradiance weighted by the phytoplankton absorption coefficient normalized to its value at 490 nm, $\mu mol\ m^{-2}\ s^{-1}$
F_f F_{fQ}	Spectral shape of fluorescence emission inside and outside the cell and scalar, nm^{-1}
K_d K	Attenuation coefficient for downwelling planar and scalar irradiance, m^{-1}
$\mathbf{K}_d^{mod}\|_{0-}^{2.75}$ $\mathbf{K}_d^{mod}\|_{0+}^{2.75}$	LUT attenuation coefficient for planar irradiance from $0-$ to 2.75 m and from 0^+ to 2.75 m, m^{-1}
L_u L_{ub} L_{uR} L_{uf} L_{uCDOM} $L_{ubottom}$	Total upwelling radiance and upwelling radiance due to backscattered photons, Raman scattered photons, chlorophyll fluorescence, CDOM fluorescence and bottom reflection, $\mu mol\ m^{-2}\ s^{-1}\ nm^{-1}\ sr^{-1}$
Q_a^*	Fraction of the fluoresced radiance not reabsorbed inside the cell, Unitless
R_L R_{Lb} R_{LR} R_{Lf} R_{LCDOM} R_{bottom}	Radiance reflectance (see L_u for subscripts), sr^{-1}
$\mathbf{R}_L^{obs}$ $\mathbf{R}_{Lb}^{mod}$ $\mathbf{R}_{Lf}^{mod}$	Vector of observed radiance reflectance and modeled backscattered and fluoresced radiance reflectance, sr^{-1}
$\mathbf{R}_{Lb}^{mod\ HL}$	LUT solution of $\mathbf{R}_{Lb}^{mod}$ before correction for shading, sr^{-1}
$\overset{o}{\mathbf{T}}^{mod}\|_{0+}^{0.65}$ $\mathbf{T}^{mod}\|_{0+}^{0-}$	LUT transmission from $E_d(0^+)$ to $\overset{o}{E}$ (0.65) and $E_d(0^+)$ to $E_d(0^-)$, Unitless
z z_{Lu} z_{Ed}	Depth, depth of upwelling radiance sensor, depth of downwelling in-water irradiance sensor, m
ε ε_{shade}	Least square fit error, and shading error, Units vary and unitless
φ_f	Quantum yield of fluorescence, photons emitted (photons absorbed)$^{-1}$
λ	Wavelength, nm
$\boldsymbol{\theta}$ $\hat{\boldsymbol{\theta}}$ θ_i	Vector of parameters, best fit vector of parameters and element of those vectors
θ_{sun}	Solar zenith angle in air, Units vary
η_F	Spectral fluorescence quantum efficiency (SFQE) function, photons emitted (photons absorbed)$^{-1}\ nm^{-1}$

plankton ($a_\phi(\lambda)$, m^{-1}), and water ($a_w(\lambda)$, m^{-1}): $a(\lambda) = a_{CDOM}(\lambda) + a_{NAP}(\lambda) + a_\phi(\lambda) + a_w(\lambda)$. Once a function has been adopted, the spectral shape and amplitude of each absorption and scattering component can be parameterized as a simple function of the fitted parameters (in vector θ) which can then be used in a nonlinear regression procedure to find the best vector of parameters, $\hat{\theta}$, to represent a measured reflectance spectrum. For some constituents the spectral shape remains constant, while for others both the shape and amplitude are allowed to vary. More specifically, the method uses a nonlinear regression where the estimated parameters (θ) define the spectral shapes and amplitudes of the IOPs, and the independent variables are the AOP spectra. In this paper, we replace the use of an analytical function for the relationship between the IOPs and AOPs with a look-up table, while retaining the use of an optimization procedure.

[11] In the inversion models developed to date, the Raman scattering term and terms for chlorophyll fluorescence and CDOM fluorescence are usually treated independently, ignored or corrected for. The rationale for our treatment of these processes in the coastal waters of Lunenburg Bay is described below.

2.2.1. Raman Scattering

[12] *Gordon* [1999] showed that Raman scattered photons can amount to an important fraction ($\sim$10%) of the upwelling radiance in the blue-green wavebands in surface waters at low chlorophyll concentrations [see also *Morel and Gentili*, 2004]. However, radiative transfer simulations of Lunenburg Bay (using Hydrolight software, Sequoia Scientific, with the *Bartlett et al.* [1998] parameterization) showed that the fraction of upwelling radiance due to Raman scattering is at most 2 to 3% for all wavelengths (generally increasing with longer wavelengths in the visible) due to the high attenuation coefficient of water in the bay. This is consistent with the results of *Morel and Gentili* [2004] for Case 1 waters with high chlorophyll concentrations. Such small increases in the upwelling radiance are within the instrumental error of the radiometer and the uncertainty in our model for the natural light field. Therefore, for the remainder of this paper we ignore this source of radiance with little consequence on our results. However, to adapt the model developed herein to clear waters, an analytical model of Raman scattering should be implemented [e.g., *Marshall and Smith*, 1990; *Pozdnyakov and Grassl*, 2003; *Sathyendranath and Platt*, 1998].

2.2.2. CDOM Fluorescence

[13] The relative influence of CDOM in Lunenburg Bay is understood by noting that at 490 nm absorption by CDOM is typically about 5 times greater than that of phytoplankton ($a_{CDOM}(490)/a_\phi(490) = 4.52 \pm 2.02$ s.d.; $n = 13$, data for MB1 mooring site in 2003), with the chlorophyll concentration generally around 0.7 mg m^{-3} $\pm$

0.74 ± 0.26; n = 15) (J. Cullen et al., unpublished manuscript). This makes it impossible to retrieve phytoplankton biomass using absorption-based algorithms of ocean color utilizing the blue and green wavebands. The problem is further exacerbated by CDOM fluorescence. A simple simulation using Hydrolight with the default CDOM quantum yield and redistribution function [see *Mobley*, 1994] for an average CDOM absorption spectrum in Lunenburg Bay showed that CDOM fluorescence covers a broad emission band centered around 490 nm where, at its maximum, it accounts for 10 to 20% of the upwelling radiance (see Results). Due to its emission spectrum, CDOM fluorescence partially "fills-up" the dip in reflectance caused by phytoplankton absorption. Accounting for this effect is very difficult due to high variability in the shape of the redistribution function [*Coble*, 1996; *Hawes*, 1992; *Mobley*, 1994; *Seritti et al.*, 1998; *Vodacek et al.*, 1994] and, to a lesser extent, variability in the quantum yield of CDOM fluorescence [*Blough and Del Vecchio*, 2002] measured in the environment. An attempt is made by *Pozdnyakov and Grassl* [2003] to generalize the effects of CDOM fluorescence on reflectance, but at the expense of ignoring changes in the spectral redistribution function with excitation wavelength. In our inversion procedure, we adopt a different approach by avoiding the blue-green spectral region where CDOM fluorescence makes an important contribution to the upwelling radiance.

2.2.3. Chlorophyll Fluorescence

[14] The fluorescence emission centered near 683 nm must be distinguished from the background of elastically (and Raman) scattered photons. This is usually done by defining as a baseline a straight line between two wavebands outside the fluorescence emission band; this baseline value is then subtracted from the signal [see *Letelier and Abbott*, 1996, and references therein]. This provides a good method for comparing fluorescence emission from waters with similar optical properties. However, the baseline is not always a good or consistent representation of the background upwelling radiance or reflectance and can lead to biases when comparing areas with very different optical properties [*Gower et al.*, 1999; *Huot et al.*, 2005]. Another method to separate the fluorescence signal from the background using inversion models has been proposed [*Culver and Perry*, 1997; *Roesler and Perry*, 1995]. In this approach, the background radiance is not assumed spectrally flat but is modeled using the IOPs obtained from the inversion. Firstly, the inversion is carried out for wavebands shorter than those influenced by chlorophyll fluorescence (up to about 650 nm) to obtain the IOPs. Then the reflectance/radiance due only to elastic scattering in the fluorescence band is modeled based on a forward reflectance model and the retrieved IOPs for this band. The differences between the measured reflectance at wavelengths greater than 650 nm and the reflectance spectrum modeled using the IOPs retrieved by the inverse model is attributed to chlorophyll fluorescence.

[15] Our approach is an incremental improvement on the methods described above. Instead of estimating fluorescence emission at one waveband or after the inversion [*Morrison*, 2003; *Roesler and Perry*, 1995], we analyze the entire reflectance spectrum simultaneously, using an analytical function to represent $R_{Lf}(\lambda, z)$. Consequently, we relate the measured signal directly to the fluorescence

of phytoplankton while simultaneously and optimally accounting for the optical properties of the surface layer.

3. Materials and Methods

3.1. Data Collection

3.1.1. AOPs

[16] Two sets of AOP data collected from optical buoys are used in this work. The first was collected in the summer of 2003 from one buoy (MB1), and is used for model development and preliminary validation; the second was collected in 2004 from three moorings (MB1, SB2, and SB3) and is used exclusively for validation. All moorings were deployed in Lunenburg Bay, Nova Scotia, Canada (more information can be found at (http://www.cmep.ca/bay).

[17] In 2003, data were collected from 4 June to 28 September for 15 minutes every 30 minutes during daylight. The optical buoy consisted of (1) a hyperspectral TSRB (spectral resolution ~3 nm, range used from 380 to 700 nm, Satlantic Inc., Nova Scotia, Canada) which measures downwelling irradiance above the surface and upwelling radiance below the surface at 0.65 m, and (2) a chain of irradiance sensors at depth measuring at 380, 443, 490 and 555 nm with 10 nm bandwidth (TACCS using OCR-504 head, Satlantic Inc., Nova Scotia, Canada) which is used to obtain the attenuation coefficients. In this paper we use only the upper sensor in this chain, which was located at 2.58 m. The median of the 15-minute acquisition period was taken and used for the inversion. Simple quality control was applied to the data to remove outliers and correct for dark values of the TSRB. As such, median values were discarded if any of the following were encountered: the 15 minute acquisition period was "highly variable" (the ratio of the standard deviation to the mean was greater than 0.005 at 600 nm); the reflectance at 555 or 700 nm was greater than 0.008 and 0.006 sr^{-1}, respectively; the downwelling irradiance at 510 nm was lower than 2 μW cm^{-2} nm^{-1}; or the zenith angle was greater than 70° (see *Zheng et al.* [2002] for a more detailed discussion of similar quality control criteria). No further processing was applied to the optical data. This data set contains 1806 reflectance and K_d spectra of which 14 have matching IOP measurements (see section 3.1.2).

[18] The 2004 data set is obtained from three similar moorings (identical except for the depth of the in-water irradiance sensors) deployed for different lengths of time between 22 April and 18 December 2004. This provided a total of 6953 reflectance spectra of which 93 have matching in situ chlorophyll data for validation. Data have been quality controlled in the same way except that "highly variable" acquisitions were not removed.

[19] For both data sets, we calculated a proxy of the diffuse attenuation coefficient directly from the mooring data using the above-surface sensor $E_d (380, 0^+)$ and the in-water sensor at depth z_{Ed}, providing $E_d (380, z_{Ed})$: $K_d (380) = -\ln [E_d (380, z_{Ed})/E_d (380, 0^+)]/z_{Ed}$. For simplicity, we will refer to this measurement as the diffuse attenuation coefficient, despite the fact that surface effects are not corrected for; the latter are accounted for in the forward model (see section 3.5). The depth z_{Ed} differed (2.5 ± 1 m) for the three moorings. Because the attenuation coefficients during some periods in 2003 showed obvious spectral inconsistencies above 380 nm

(e.g., $K_d(555)$ much higher than $K_d(443)$), we did not use the wavebands at 443, 490 or 555 nm.

3.1.2. IOPs and Chlorophyll

[20] The IOPS measured at our study site, Lunenburg Bay, were used in four ways: (1) to define the range of values (plus some margin) to be included in a look-up table used in the model; (2) to determine the mean backscattering ratio (b_b/b) to be used for all Hydrolight simulations; (3) to obtain the mean shapes for absorption by phytoplankton and nonalgal particles plus CDOM for use during the inversion; and (4) to validate the output of the inversion model.

[21] The IOP sampling occurred approximately weekly onboard the R/V UStar. During sampling, two instrument packages were deployed: an "optical" package, which included an ac-9 (WET Labs Inc., Oregon, United States) and a Hydroscat-6 (HOBI Labs Inc., Arizona, United States), and a "physical" package which had a CTD. Just before or after these deployments, water samples were collected using a Niskin bottle at 1 m. The AOP spectra from the mooring were matched with the time of sampling of the discrete samples by taking the first median spectrum that passed the quality control criteria following the sampling time (i.e., after the optical sensors were cleaned, thus avoiding biofouling effects).

[22] The CDOM and particulate (detritus and phytoplankton; quantitative filter technique) absorption coefficients were obtained according to the NASA satellite validation protocols [*Pegau et al.*, 2003] using a dual beam spectrophotometer.

[23] The scattering coefficient was measured using the ac-9 and processed according to the manufacturer's protocol (using a spectrally resolved scattering correction, their method #3). Temperature and salinity corrections were made using data from a near-simultaneous CTD cast.

[24] The backscattering coefficients were obtained using the Hydroscat-6 deployed on the same package as the ac-9 and were processed according to *Boss and Pegau* [2001]. The spectrally interpolated results from the ac-9 were used to obtain the path attenuation correction (i.e., sigma correction [see *Maffione and Dana*, 1997]).

[25] The chlorophyll and phaeopigment concentrations were obtained by fluorescence using the acid ratio method and extraction in 90% acetone [*Mueller et al.*, 2003]. We report the mean of triplicate samples.

3.1.3. Laboratory Measurement of Fluorescence Emission

[26] For reasons given later, we used a fluorescence emission shape measured in the laboratory. The fluorescence spectral shape used during the inversion (F_{fQ} in equation (12), below) was determined by illuminating an optically thin, nutrient replete, high light grown culture (~1000 μmol m^{-2} s^{-1}) of *Thalassiosira pseudonana* (Figure 6) with a broadband blue light and using a spectroradiometer (USB2000, Ocean Optics Inc., United States; spectrally calibrated using a NIST-traceable light source; LS-1-CAL, Ocean Optics Inc., United States) to measure the emission spectrum. The culture was grown in semicontinuous turbidostat mode [e.g., *MacIntyre and Cullen*, 2005], illuminated with blue fluorescent tubes (65 W Ultra-Actinic, Customsealife Inc.) and diluted once per day. To avoid carbon limitation, the biomass was kept below 80 mg chl m^{-3}.

The measurement was carried out following a dilution and was made at 90° from the growth irradiance.

3.2. Overview of the Inverse Model

[27] Our primary objective is to retrieve phytoplankton absorption or chlorophyll concentration, both proxies for phytoplankton biomass, from autonomous observations of reflectance and the diffuse attenuation coefficient in surface waters. Phytoplankton biomass is estimated from Sun-induced fluorescence detected in the red wavelengths of the reflectance spectrum by: (1) using an inverse model of reflectance and the attenuation coefficient to retrieve the optical properties of the water that must be known to correct the fluorescence signal for backscattered radiance and the transmission of sunlight and fluoresced photons in the upper water column [e.g., *Babin et al.*, 1996b]; and (2) assigning a relationship between the quantum yield of fluorescence and irradiance to calculate phytoplankton absorption from fluorescence. Thus, in addition to retrieving estimates of phytoplankton absorption (which can be related to chlorophyll), the model also provides an estimate of the sum of CDOM and detritus absorption and the backscattering coefficients, as well as spectral estimates of reflectance and attenuation that can be compared to measurements for model validation. A diagram of the inverse model is provided in Figure 1 and its parameterization is summarized in Table 2. The reader should become familiar with both before proceeding.

[28] We constructed a forward model to reproduce apparent optical properties measured in situ as a function of solar radiation and a range of IOPs: instead of correcting the measurements to obtain "standard" optical measurements (such as remote sensing reflectance), we construct the model to reproduce the light field observed for the geometry of the measuring instrument.

[29] The forward model is built in two parts:

[30] 1. The first part describes the elastic component of the light field and is based on look-up tables (LUTs) derived from radiative transfer simulations. The inputs used to create these tables are the IOPs and the solar zenith angle while the outputs are AOPs. Three LUTs are used for the elastic component, two to describe K_d and one for R_{Lb}. The look-up tables are general and do not include any assumptions about the shape of the absorption or scattering constituents, they do, however, use a constant backscattering ratio for particles, 0.0144, which is the mean of the measurements from the study area. We chose to use LUTs rather than an analytical model to provide us with an accurate description of the light field for different solar zenith angles (important in a system that measures throughout the day) and for a wide range of wavelengths (380 to 700 nm). In this sense, the approach is similar to that used by *Morel et al.* [2002] to correct remote sensing reflectance for the bidirectional effects of the observation geometry.

[31] 2. The second part, describing fluorescence emission, is built around an analytical function similar to those used by *Morrison* [2003] and *Maritorena et al.* [2000], but it also uses some output from the LUTs to calculate the attenuation coefficient and the scalar irradiance at 0.65 m.

[32] To model the AOPs detected by the instruments more accurately, we apply a correction to the forward model to account for the shading produced by the instrument (i.e., the effect of shading is added to the theoretical model and not
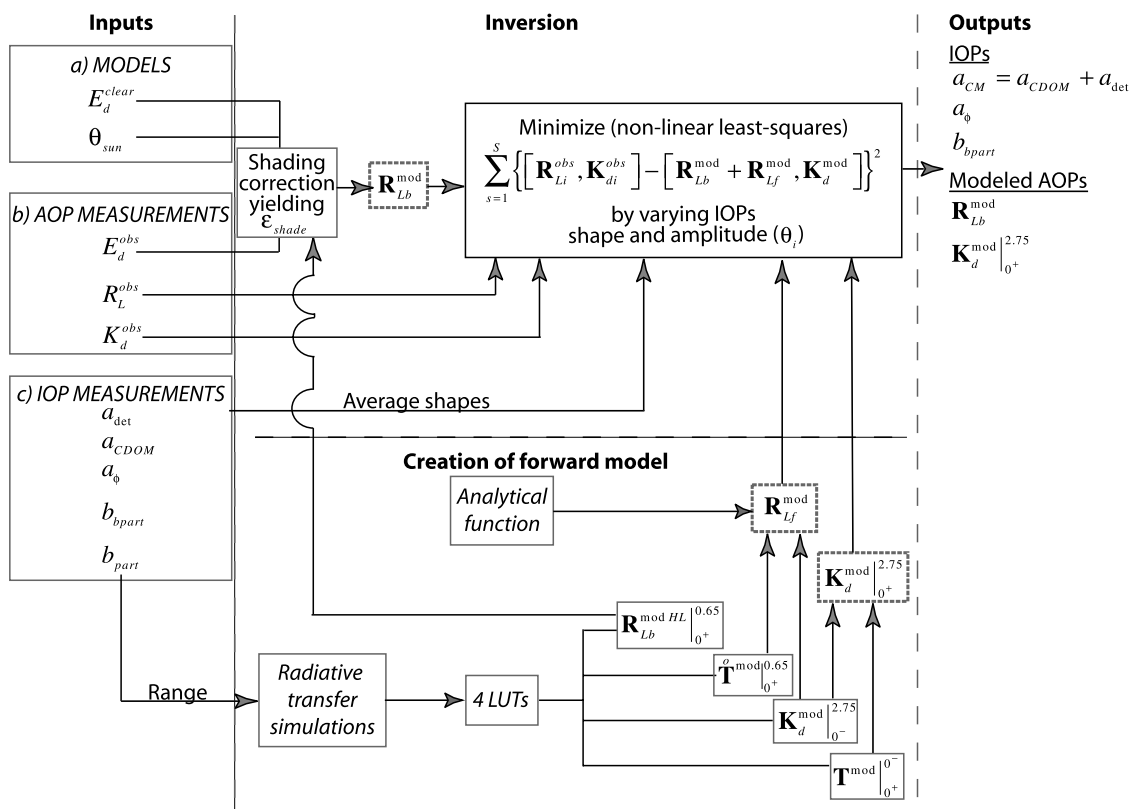
Figure 1. Schematic representation of the inverse model. The diagram is divided into four sections: the inputs (left), the creation of the forward model (bottom center), the inversion (top center), and the outputs (right). Dependence on wavelength is omitted to simplify the notation. Input: Three types of inputs are used in the model: (a) models — the incident irradiance under clear sky conditions (E_d^{clear}) and the solar zenith angle (θ_{sun}) are calculated for the location and time of the AOP measurements; (b) AOPs measured by the floating radiometer buoy and K-chain — spectra of incident irradiance (E_d^{obs}), reflectance (upwelling radiance at 0.65 m divided by downwelling irradiance above the surface, $\mathbf{R}_L^{obs}$), and the attenuation coefficient ($\mathbf{K}_d^{obs}$) calculated from measurements of downwelling irradiance above the surface and at depth z_{Ed}, about 2.75 m; (c) IOPs; measured during field trips to the moorings sites. They are used: (i) for defining the IOPs ranges for the creation of the forward model; (ii) for defining average spectral shapes for absorption used during the inversion; and (iii) for the validation of the model outputs (not represented here). Creation of forward model: Four look-up tables (LUTs) based on the range of IOPs measured in the waters of Lunenburg Bay are created and used in the forward model to describe three AOPs ($\mathbf{R}_{Lb}^{mod}$, $\mathbf{K}_d^{mod}|_{0^+}^{2.75}$, $\mathbf{R}_{Lf}^{mod}$, thick dashed boxes) in terms of IOPs and the solar zenith angle. The first two ($\mathbf{R}_{Lb}^{mod}$, $\mathbf{K}_d^{mod}|_{0^+}^{2.75}$) are defined solely based on the LUTs constructed using a series of radiative transfer simulations (Hydrolight). The effect of instrument self-shading (see Appendix B) is applied to the LUT reflectance model ($\mathbf{R}_{Lb}^{mod\ HL}$) to obtain $\mathbf{R}_{Lb}^{mod}$ and to reproduce more closely the measurements before the inversion. The third AOP, reflectance due to fluorescence ($\mathbf{R}_{Lf}^{mod}$), is based on an analytical function but uses outputs from the LUT table. Inversion: The inversion involves minimizing the differences between the measured and modeled AOPs by modifying the IOPs' magnitude (and shape in the case of b_{bpart}). Outputs: The outputs of the inversion are three IOPs: a_ϕ, a_{CM}, and b_{bpart}. Additionally, the outputs from the look-up tables (AOPs) using the retrieved IOPs as inputs are also available. The validation of the model is done by comparing the outputs with a validation data set of measured IOPs.

removed from the measurements; see Appendix B). The inversion finds the combination of optical properties that, when applied in the forward model, best reproduces measured AOPs, including fluorescence emission as detected in red reflectance; it is carried out by changing a total of four parameters in the forward model to minimize the differences between the measured vs. modeled reflectance and attenuation coefficient: two parameters describing the amplitudes of IOP spectral shapes (phytoplankton absorption, a_ϕ and absorption by the sum of CDOM and nonalgal particulates, $a_{CM} = a_{CDOM} + a_{NAP}$); and two parameters describing the amplitude and spectral shape of backscattering by particles, b_{bpart}. A function is obtained and used to describe the decrease in the quantum yield of fluorescence at high irradiance due to nonphotochemical quenching. In the inversion, this quantum yield, applied to retrieved fluores-

Table 2. Parameterization of the Inverse Model

Description	Model
Number of fitted parameters	4 ($\theta_{1\ldots4}$); in spectral shape equations below
IOPs retrieved	Phytoplankton absorption (a_ϕ), the sum of CDOM and nonalgal particles absorption (a_{CM}), the backscattering coefficient of particles (b_{bpart})
Spectral shapes	$a_\phi(\lambda) = \theta_1\ \bar{a}_\phi^{490}(\lambda)$ $= a_\phi(490)\ \bar{a}_\phi^{490}(\lambda)$ $a_{CDOM}(\lambda) = \theta_2\ \bar{a}_{CDOM}^{400}(\lambda)$ $= a_{CDOM}(400)\ \bar{a}_{CDOM}^{400}(\lambda)$ $b_{bpart}(\lambda) = \theta_3\ (\lambda/650)^{-\theta_4}$ $= b_{bpart}(650)\ (\lambda/650)^{-sbpart}$
Wavebands fitted	$R_{\rm L}$: 380 to 400 (9 wavebands) and 605 to 700 nm (28 wavebands) $K_{\rm d}$: 380 nm (1 waveband)
AOPs used	Downwelling irradiance ($E_d(0^+)$), reflectance (R_L) and diffuse attenuation (K_d)
Model inputs	Solar zenith angle for all LUTs (θ_{sun}) and the ratio of diffuse to direct planar irradiance for the shading correction (ε)
Quantum yield	A function of scalar PUR irradiance at 0.65 m (E_{PUR}^{490})

cence emission, constrains the estimate of phytoplankton absorption.

3.3. General Formulation

[33] The reflectance model is the sum of two contributions, one from backscattered radiance and one from chlorophyll fluorescence: $R_L(\lambda, z) = R_{Lb}(\lambda, z) + R_{Lf}(\lambda, z)$. Therefore, our model does not include Raman scattering, CDOM fluorescence, or bottom reflection processes (see equation (2)).

[34] Most inverse models work by minimizing the sum of the squared differences (or another cost function) between the observed radiance reflectance vector ($\mathbf{R}_L^{\rm obs}(\lambda)$, sr^{-1}) and the forward reflectance model ($\mathbf{R}_{Lb}^{\rm mod}(\lambda|\boldsymbol{\theta})$, sr^{-1}), a vector-valued function. This is accomplished by varying the V parameters in the vector of parameters $\boldsymbol{\theta} = [\theta_1,\ldots,\theta_V]$, which define the amplitudes and spectral shapes of J spectral components $\phi(\lambda|\boldsymbol{\theta})$. The dependency notation should be read "of lambda given the vector of parameters theta". These J spectral components are separated into two types, those that correspond to backscattering $\phi_{bj}(\lambda|\boldsymbol{\theta})$ and those that correspond to absorption $\phi_{aj}(\lambda|\boldsymbol{\theta})$ of the jth component. With this notation $\phi_{a1}(\lambda|\boldsymbol{\theta})$ could be used, for example, to represent the spectral absorption of phytoplankton, which would be the product of a phytoplankton absorption vector normalized to 490 nm $\bar{\mathbf{a}}_\phi^{490}(\lambda)$ (unitless) and an amplitude θ_1(m^{-1}) corresponding to the absorption at 490 nm, such that $\phi_{a\phi}(\lambda|\boldsymbol{\theta}) = \mathbf{a}_\phi(\lambda) = \theta_1\ \bar{\mathbf{a}}_\phi^{490}(\lambda)$.

[35] The reconstructed total absorption and backscattering coefficients then become:

$$\begin{aligned} \mathbf{a}(\lambda|\boldsymbol{\theta}) &= \sum_{j=1}^{J} \phi_{aj}(\lambda|\boldsymbol{\theta}) \\ \mathbf{b}_b(\lambda|\boldsymbol{\theta}) &= \sum_{j=1}^{J} \phi_{bj}(\lambda|\boldsymbol{\theta}) \end{aligned} \qquad (4)$$

[36] The general formulation with fluorescence is obtained simply by adding the modeled fluorescence vector valued function ($\mathbf{R}_{Lf}^{\rm mod}(\lambda|\boldsymbol{\theta})$, sr^{-1}), developed below (see equation (9)), which leads to the general model for the regression of the ith measured reflectance spectrum ($\mathbf{R}_{Li}^{\rm obs}(\lambda)$),

$$\mathbf{R}_{Li}^{\rm obs}(\lambda) = \mathbf{R}_{Lb}^{\rm mod}(\lambda|\boldsymbol{\theta}_i) + \mathbf{R}_{Lf}^{\rm mod}(\lambda|\boldsymbol{\theta}_i) + \varepsilon_i(\lambda) \qquad (5)$$

where $\varepsilon(\lambda)$ is a vector of errors. The least squares cost function becomes

$$\sum_{s=1}^{S} \left\{ \mathbf{R}_{Li}^{\rm obs}(\lambda_s) - \left[\mathbf{R}_{Lb}^{\rm mod}(\lambda_s|\boldsymbol{\theta}_i) + \mathbf{R}_{Lf}^{\rm mod}(\lambda_s|\boldsymbol{\theta}_i) \right] \right\}^2, \qquad (6)$$

where λ_s is the $s^{\rm th}$ wavelength and reflectance is measured with a total of S wavelengths. An optimization procedure is used to minimize the square of the differences between the measured and modeled reflectance spectra to obtain the estimated parameters $\hat{\boldsymbol{\theta}}_i$. In our case, the inversion is performed for both the attenuation coefficient and reflectance such that we create a new vector $[\mathbf{R}_{Li}(\lambda_s), \mathbf{K}_{di}(\lambda_s)]$ on which the inversion procedure is carried out with the same minimization of squares:

$$\begin{aligned} \sum_{s=1}^{S} \mathbf{w}_i(\lambda_s) &\Big\{ \left[\mathbf{R}_{Li}^{obs}(\lambda_s), \mathbf{K}_{di}^{obs}(\lambda_s) \right] - \left[\mathbf{R}_{Lb}^{\rm mod}(\lambda_s|\boldsymbol{\theta}_i) \right. \\ &\left. + \mathbf{R}_{Lf}^{\rm mod}(\lambda_s|\boldsymbol{\theta}_i), \mathbf{K}_{d}^{\rm mod}(\lambda_s|\boldsymbol{\theta}_i) \right] \Big\}^2. \end{aligned} \qquad (7)$$

where $\mathbf{w}_i$ is a vector of weights. The relative error between the model and measurements is expected to be similar for the attenuation and reflectance. However, the variance is different because values of K_d are $\sim10-100$ times larger than R_L. Therefore, a weighted least squares approach is necessary. To account for the difference in variance, we first weight by the inverse square of the value of the measurement ($1/y^2$ weightings). Two other factors were taken into account when adjusting the weights: (1) the number of points (wavelength, λ_s) for each measurement (N_{R_L} and N_{K_d}), and (2) the information content of the measurement (not all wavebands are independent). We assume that K_d, which is

Table 3. Parameterization and Construction of the Look-Up Tables for $\mathbf{R}_{LB}^{\mathrm{mod}}|_{0+}^{0.65}$, $\mathbf{T}^{\mathrm{mod}}|_{0+}^{0-}$, $\mathbf{K}_d^{\mathrm{mod}}|_{0-}^{2.75}$, and $\overset{o}{\mathbf{T}}{}^{\mathrm{mod}}|_{0+}^{0.65}$

Variable	Values of Input for Hydrolight Simulation
a_{nw}, m^{-1}	0, 0.005, 0.025, 0.05, 0.075, 0.1, 0.15, 0.2, 0.3, 0.4, 0.5, 0.625, 0.75, 1.0, 1.25, 1.5, 1.75, 2.0, 2.25, 2.5, 2.75, 3.0, 3.25 (independent of wavelength)
b_{bnw}, m^{-1}	0.0001, 0.0007, 0.0014, 0.0029, 0.005, 0.0072, 0.0144, 0.0216, 0.0288, 0.036, 0.0432, 0.0504 (independent of wavelength)
θ_{sun}, degrees	11.2, 20.6, 30.4, 40.3, 50.2, 60.1, 70.1, 80.0
λ, nm	Every 5 nm from 377.5 to 702.5 nm
Atmosphere	*Gregg and Carder* [1990] irradiance model with: Pressure = 101.3 Mpa, Air mass type = 1.0, Relative Humidity = 80.0 %, Precipitable water = 2.5 cm, 24-hr wind speed = 3.0 m/s, Current wind speed = 3.0 m/s, Visibility = 15.0 km, Total ozone = 392.0 Dobson units Clouds: no clouds; radiance distribution: Harrison and Coombes [*Harrison and Coombes*, 1988];
Ocean	IOPs depth distribution: constant; IOPs spectral shape: constant (except water); Water depth: infinite; Raman scattering: off; chlorophyll fluorescence: off; CDOM fluorescence: off; particle scattering phase function backscattering ratio: 0.0144

analyzed only at 380 nm (Table 2), contains information only about a_{CM} (where $a_{CM} = a_{CDOM} + a_{NAP}$), while R_L contains information on b_{bpart} (θ_3 and θ_4, see below) and a_ϕ and a_{CM}. This leads to the weight for reflectance as $[4(N_{K_d}/N_{R_L})$ $(1/\mathbf{R}_L^{obs})]^2$. For the K_d measurements $(1/\mathbf{K}_d^{obs})^2$ is used for the weight. Therefore, we used

$$\mathbf{w} = \left[\left[4(N_{K_d}/N_{R_L})(1/\mathbf{R}_L^{obs}) \right]^2, (1/\mathbf{K}_d^{obs})^2 \right].$$

[37] Hence, in both cases, the variance is normalized to the value of the measurement. In summary, the weight of reflectance is reduced in proportion to the number of wavebands used relative to those used for K_d while it is multiplied by 4 because it contains about four times as much information. This weighting is intended to provide equal weighting to the attenuation and reflectance, while accounting for the nonindependence of the wavebands in the reflectance spectra by reducing their weights (N_{K_d}/N_{R_L}). In this section, for the formal statistical setup of the problem we use have used a vectorial notation, which allows a more formal description of the problem. However, for the remainder of the paper we will use this notation more loosely. All optimization procedures were carried out in MATLAB$^{\circledR}$ (The Mathworks Inc., United States), using a bounded nonlinear least squares approach [*Coleman et al.*, 2000; *Coleman and Li*, 1994]. The upper bounds were set high enough to never influence the fit while the lower bounds were set to 0 for all parameters except for θ_4, the exponent of the power function describing the spectral dependence of backscattering, which was bounded at -1. This allows for the possibility of absorbing particles or monodispersed particles influencing the shape of the backscattering curve (see below).

3.4. Description of the Look-Up Tables

[38] As mentioned before, look-up tables are used to describe the elastic scattering component of the model and some aspects of the fluorescence model. These tables were created by running a series of Hydrolight simulations encompassing the range of absorption, scattering and solar zenith angles expected in Lunenburg Bay, i.e., the measured range plus some margin. Details of the Hydrolight runs are given in Appendix A (see also Table 3). Briefly, Hydrolight was run with the IOPs for water plus variable amounts of absorption and scattering by "nonwater" material. The "nonwater" material had spectrally flat scattering and

absorption coefficients. This allows the creation of look-up tables which are general and monotonic for all independent variables. Outputs were saved every 5 nm from 377.5 to 702.5 nm at 0, 0.65 and 2.75 m below the surface. A look-up table was then created with four independent (input) variables, $a_{nw}(\lambda) = a(\lambda) - a_w(\lambda)$, $b_{bnw}(\lambda) = b_b(\lambda) - b_{bw}(\lambda)$, θ_{sun} and λ, where the subscript "nw" stands for "nonwater". The dependent variables are: (1) a TSRB-like reflectance, which consists of the ratio of the upwelling radiance at 0.65 m to downwelling irradiance above the surface, $\mathbf{R}_{Lb}^{\mathrm{mod}\ HL}(\lambda|a_{nw}, b_{bnw}, \theta_{sun})|_{0+}^{0.65} = L_u(\lambda, 0.65)/E_d(\lambda, 0^+)$; (2) the ratio of planar irradiance below the surface to that above the surface, $\mathbf{T}^{\mathrm{mod}}(\lambda|a_{nw}, b_{bnw}, \theta_{sun})|_{0+}^{0-} = E_d(\lambda, 0^-)/E_d(\lambda, 0^+)$; (3) the attenuation coefficient for planar irradiance from just below the surface to 2.75 m, $\mathbf{K}_d^{\mathrm{mod}}(\lambda|a_{nw}, b_{bnw}, \theta_{sun})|_{0-}^{2.75}$; (4) the ratio of the scalar irradiance at 0.65 m to the planar irradiance above the surface, $\overset{o}{\mathbf{T}}{}^{\mathrm{mod}}(\lambda|a_{nw}, b_{bnw}, \theta_{sun})|_{0+}^{0.65} = \overset{o}{E}(\lambda, 0.65)/E_d(\lambda, 0^+)$. Further details for each of these LUTs follow below.

3.5. Description of $\mathbf{R}_{Lb}^{\mathrm{mod}}(\lambda|\theta)$

[39] The look-up table for $\mathbf{R}_{Lb}^{\mathrm{mod}\ HL}(\lambda|a_{nw}, b_{bnw}, \theta_{sun})|_0^{0.65}$ corrected for shading (see Appendix B), is the model used for the inversion of reflectance resulting from elastic scattering (equation (7)): $\mathbf{R}_{Lb}^{\mathrm{mod}}(\lambda|\theta) = [1 - \varepsilon_{shade}(\lambda|\theta)]\mathbf{R}_{Lb}^{\mathrm{mod}\ HL}(\lambda|\theta)$ where $\varepsilon_{shade}(\lambda|\theta)$ is a vector of shading errors.

3.6. Description of $\mathbf{K}_d^{\mathrm{mod}}(\lambda|\theta)$

[40] The look-up tables for $\mathbf{T}^{\mathrm{mod}}(\lambda|a_{nw}, b_{bnw}, \theta_{sun})|_{0+}^{0-}$ and $\mathbf{K}_d^{\mathrm{mod}}(\lambda|a_{nw}, b_{bnw}, \theta_{sun})|_{0-}^{2.75}$ are used during the inversion of the TSRB/TACCS attenuation coefficient, which uses the above surface irradiance and the downwelling irradiance at z_{Ed} to derive an attenuation coefficient which incorporates the air-sea interface effects (section 3.1.1): $\mathbf{K}_d^{\mathrm{mod}}(\lambda|\theta)|_{0+}^{2.75}$. To allow for more versatility in terms of the depth of the in-water sensor, we separate the model into an interface transmission term and a water attenuation term:

$$\mathbf{K}_d^{\mathrm{mod}}(\lambda|\theta)|_{0+}^{2.75} = \frac{1}{2.75}\ln(E_d(0^+)/E_d(2.75))$$

$$= \frac{1}{2.75}\ln([E_d(0^+)/E_d(0^-)][E_d(0^-)/E_d(2.75)])$$

$$= \frac{1}{2.75}\ln(E_d(0^-)/E_d(2.75)) - \frac{1}{z_{Ed}}\ln(E_d(0^-)/E_d(0^+))$$

$$= \mathbf{K}_d^{\mathrm{mod}}(\lambda|\theta)|_{0-}^{2.75} - \frac{1}{z_{Ed}}\ln\left(\mathbf{T}^{\mathrm{mod}}(\lambda|\theta)|_{0+}^{0-}\right). \quad (8)$$

[41] We now give the rationale for replacing $1/2.75$ by z_{Ed} on the third line of equation (8). Changing the depth of the in-water downwelling irradiance sensor will not lead to large changes for a hypothetical attenuation coefficient calculated from just below the surface to that depth (first term last line of equation (8)) we therefore use a LUT made for one depth (2.75 m). The term including the transmission across the interface (though small) is inversely proportional to the depth of the sensor (second term last line of equation (8)), we therefore use z_{Ed} as well as a constant LUT when modeling the effect of transmission on the mooring measurements of K_d. In other words, since z_{Ed} depends on the configuration of the mooring, and because K_d is not expected to change much with small changes in z_{Ed}, separating the LUT into two terms (instead of only one term for $\mathbf{K}_d^{\mathrm{mod}}(\lambda)|_{0+}^{2.75}$) allows us to keep the same LUT for $\mathbf{K}_d^{\mathrm{mod}}(\lambda)|_{0-}^{2.75}$ and $\mathbf{T}^{\mathrm{mod}}(\lambda)|_{0+}^{0-}$ and change only z_{Ed} in front of the second term to obtain a more accurate description.

3.7. Equation for the Upwelling Fluorescence Radiance Used in the Inverse Model

[42] Assuming a homogeneous water column with respect to the IOPs, the upwelling radiance at wavelength λ and depth z_{Lu} due to fluorescence emission in the ocean can be modeled as follows [e.g., Babin et al., 1996a; Maritorena et al., 2000; Mobley, 1994],

$$L_{uf}(\lambda, z_{Lu}) = \frac{1}{4\pi}Q_a^*(\lambda)\int_{400}^{700}\int_{z_{Lu}}^{\infty}a_\phi(\lambda_{ex})\eta^F(z, \lambda_{ex} \to \lambda)$$
$$\cdot \overset{\circ}{E}(\lambda_{ex}, z_{Lu})e^{-[K(\lambda_{ex})+a_f(\lambda)](z-z_{Lu})}\,dz\,d\lambda_{ex}, \quad (9)$$

where Q_a^* is the fraction of light emitted inside the cell and not reabsorbed, η^F (nm^{-1}) is the spectral fluorescence quantum efficiency (SFQE) function for irradiance absorbed at waveband λ_{ex} by all cellular pigments and reemitted at the emission wavelength λ (nm^{-1}), $\overset{\circ}{E}$ is the scalar irradiance, K is the diffuse attenuation coefficient for scalar irradiance, and a_f is the attenuation coefficient for fluoresced upwelling radiance.

[43] To simplify the problem, the SFQE function is often assumed independent of depth: $\eta^F(z, \lambda_{ex} \to \lambda) = \eta^F(\lambda_{ex} \to \lambda)$ thus allowing us to take η^F outside the depth integral, and to carry out the depth integration:

$$L_{uf}(\lambda, z_{Lu}) = \frac{1}{4\pi}Q_a^*(\lambda)\int_{400}^{700}\eta^F(\lambda_{ex} \to \lambda)\frac{a_\phi(\lambda_{ex})\overset{\circ}{E}(\lambda_{ex}, z_{Lu})}{K(\lambda_{ex})+a_f(\lambda)}\,d\lambda_{ex}. \quad (10)$$

[44] The problem can be simplified by noting that in reality the spectral shape of emission (but not the magnitude) is independent of the excitation wavelength, such that we can conveniently express the SFQE function as $\eta^F(\lambda_{ex} \to \lambda) = \varphi_f(\lambda_{ex})F_f(\lambda)$, where $F_f(\lambda)$ is a constant emission spectral shape (nm^{-1}) and $\varphi_f(\lambda_{ex})$ is the quantum yield of fluorescence, operationally defined as the number of photons emitted at all wavelengths divided by the absorbed irradiance at wavelength λ_{ex} by all cellular pigments.

[45] It is well documented that, at least in some species, the quantum yield of fluorescence for algal cells, as operationally defined here, varies, sometimes strongly, with the excitation wavelength. This is due to the relative pigment composition of the strongly fluorescing photosystem II and weakly fluorescing photosystem I, and the spectrally varying ratio of photosynthetic to photoprotective pigments [Johnsen et al., 1997; Loftus and Seliger, 1975; Lutz et al., 1998; Raateoja et al., 2004; SooHoo et al., 1982]. For convenience, we will follow the assumption generally made in ocean optics research that the quantum yield is independent of excitation wavelength: $\eta^F(\lambda_{ex} \to \lambda) = \varphi_f(\lambda_{ex})F_f(\lambda) = \varphi_f F_f(\lambda)$. This assumption allows the simplification of equation (10) leading to our depth-integrated radiance fluorescence equation:

$$L_{uf}(\lambda, z_{Lu}) = \frac{1}{4\pi}Q_a^*(\lambda)F_f(\lambda)\varphi_f\int_{400}^{700}\frac{a_\phi(\lambda_{ex})\overset{\circ}{E}(\lambda_{ex}, z_{Lu})}{K(\lambda_{ex})+a_f(\lambda)}\,d\lambda_{ex}. \quad (11)$$

3.7.1. Approach for Constraining the Depth-Integrated Fluorescence Equation During the Inversion

[46] Starting from equation (11), we need to express $Q_a^*(\lambda)$, $F_f(\lambda)$, $\overset{\circ}{E}(\lambda, z_{Lu})$, $K(\lambda)$ and $a_f(\lambda)$ in terms of $a_{nw}(\lambda) = a_\phi(\lambda) + a_{CM}(\lambda)$, $b_{bnw}(\lambda)$, and θ_{sun}, which are inputs into the look-up table. Furthermore, $a(\lambda)$ and $b_b(\lambda)$ have to be described in terms of the model parameters $[\theta_1, \ldots, \theta_V]$ (Table 2). We now provide an overview of these terms before giving a more detailed description of the spectral shapes.

[47] For the present model, the reabsorption term, $Q_a^*(\lambda)$, is combined with the $F_f(\lambda)$ spectral shape of emission and assumed invariant: $F_{fQ}(\lambda) = Q_a^*(\lambda)F_f(\lambda)$ (nm^{-1}). This can be achieved by using the chlorophyll a fluorescence emission spectrum obtained from a representative algal culture (see Results) for $F_{fQ}(\lambda)$. The parameter $\overset{\circ}{E}(\lambda, 0.65)$ is modeled by multiplying the measured incident irradiance, $E_d(\lambda, 0^+)$, by the look-up table value for $\overset{\circ}{\mathbf{T}}^{\mathrm{mod}}|_{0+}^{0.65}$. It is assumed that the scalar irradiance attenuation coefficient, K, is the same as the planar attenuation coefficient and is modeled using the look-up table for $\mathbf{K}_d^{\mathrm{mod}}(\lambda)|_{0-}^{2.75}$. Unless the measurement is made in a highly scattering environment, the attenuation coefficient for the attenuation of upwelling fluorescence radiance $a_f(\lambda)$ can be approximated by $a_f(\lambda) = a(\lambda) = a_w(\lambda) + a_\phi(\lambda) + a_{CM}(\lambda)$. For the inversion, $a_\phi(\lambda)$ is replaced by the estimated spectral shape $\phi_{a\phi}(\lambda|\theta)$ and $a_{CM}(\lambda)$ is replaced by $\phi_{aCM}(\lambda|\theta)$ (see equation (4) and section 3.8.1).

3.7.2. Final Fluorescence Reflectance Model

[48] The depth-integrated fluorescence equation (11) describes the upwelling fluorescence radiance. By dividing equation (11) by the irradiance measured above the surface to obtain reflectance and replacing the terms $Q_a^*(\lambda)F(\lambda)$ by $F_{fQ}(\lambda)$, $\overset{\circ}{E}(\lambda_{ex}, 0.65)$ by $E_d(\lambda_{ex}, 0^+)\overset{\circ}{\mathbf{T}}^{\mathrm{mod}}|_{0+}^{0.65}$, $a_\phi(\lambda)$ by $\phi_{a\phi}(\lambda|\theta)$, and $a_{CM}(\lambda)$ by $\phi_{aCM}(\lambda|\theta)$ we have an appropriate model for the TSRB fluorescence reflectance that is expressed as

$$\mathbf{R}_{Lf}^{\mathrm{mod}}(\lambda, 0.65) = \frac{F_{fQ}(\lambda)\varphi_f}{4\pi E_d(\lambda, 0^+)}$$
$$\cdot\int_{400}^{700}\frac{\phi_{a\phi}(\lambda_{ex})E_d(\lambda_{ex}, 0^+)\overset{\circ}{\mathbf{T}}^{\mathrm{mod}}|_{0+}^{0.65}}{\mathbf{K}_d^{\mathrm{mod}}(\lambda_{ex})|_{0-}^{2.75} + (a_w(\lambda) + \phi_{aCM}(\lambda) + \phi_{a\phi}(\lambda))}\,d\lambda_{ex}, \quad (12)$$

where $F_{fQ}(\lambda)$ is normalized such that $\int_0^\infty F_{fQ}(\lambda)d\lambda = 1$, hence, the quantum yield obtained by the inversion is defined in terms of the fluorescence emitted from the cell over all emission wavelengths. Both sides of equation (12) are implicitly dependent on θ. We now describe the spectral shapes used and the wavelengths inverted.

3.8. Location-Specific Considerations

3.8.1. Spectral Shapes in Lunenburg Bay

[49] The model has 4 fitted parameters and 3 spectral shapes (see Table 2). The spectral shapes for absorption by phytoplankton and colored matter are kept constant at the mean values measured in Lunenburg Bay during the weekly sampling conducted from June 2003 through September 2003, which showed limited spectral variability:

$$a_\phi(\lambda) = \phi_{a\phi} = \theta_1 \bar{a}_\phi^{490}(\lambda), \qquad (13)$$

and

$$a_{CM}(\lambda) = \phi_{aCM} = \theta_2 \bar{a}_{CM}^{400}(\lambda), \qquad (14)$$

where $\bar{a}_\phi^{490}(\lambda)$ and $\bar{a}_{CM}^{400}(\lambda)$, are the average spectra for phytoplankton and nonalgal colored matter normalized to 490 and 400 nm, respectively. The backscattering spectrum is given by

$$b_{bpart}(\lambda) = \phi_{bpart} = \theta_3 \left(\frac{\lambda}{650}\right)^{-\theta_4}, \qquad (15)$$

where θ_3 is the backscattering coefficient by particles at 650 nm ($b_{bpart}(650)$) and θ_4 is the spectral decrease of the power function used to describe backscattering (closer to 1– 2 for small particles and closer to 0 for large particles [e.g., *Morel and Maritorena*, 2001]). The absorption by water was taken from *Pope and Fry* [1997].

3.8.2. Wavebands Used in the Inversion

[50] In Lunenburg Bay, as in many coastal environments, absorption and fluorescence by CDOM as well as bottom reflectance can interfere with the detection of phytoplankton when using information in the blue-green region of the spectrum. In contrast, at the red end of the spectrum, where phytoplankton fluorescence occurs, absorption by water is very strong, so bottom reflectance and both fluorescence and absorption by CDOM are negligible. This allows the chlorophyll fluorescence spectrum and amplitude to be estimated with minimal interference from other optical constituents [*Roesler and Perry*, 1995]. Therefore, the fluorescence band is useful for the retrieval of phytoplankton biomass in terms of absorption for these waters (see equation (11)) if the quantum yield is near constant or its variability can be predicted. In addition in the bands above ~600 nm but below ~660 nm where fluorescence emission begins, variability in the water reflectance originates mostly from variability in the backscattering coefficient. ln the shorter wavebands, below ~400 nm, the attenuation of irradiance is mostly due to CDOM absorption, and CDOM fluorescence and bottom reflectance are negligible due to the high attenuation coefficients (and reduced incident excitation irradiance for CDOM fluorescence). Estimates of CDOM absorption made using the near UV allow the

retrieval of a dominant source of absorption, hence attenuation, in the blue-green wavebands. Having recognized the benefits of analyzing the red region of the spectrum and avoiding the blue-green wavelengths, we designed our model to fit only the wavebands from 380 to 400 nm and 605 to 700 nm for R_L, and the 380 nm waveband for K_d.

4. Results

[51] The high-frequency AOP measurements from the MB1 optical mooring during the summer of 2003 as well as the weekly discrete absorption data are shown in Figure 2. The incident PAR irradiance above the surface measured with the hyperspectral TSRB (Figure 2a) illustrates that most days were sunny with a midday irradiance of around 2000 μmol m^{-2} s^{-1}, while a cloudy period — which also coincided with strong rain events — is observed at the beginning of August. Later, we will examine this time period for diel variability. The 555 to 443 nm reflectance ratio is relatively stable for the whole deployment except for the heavy rain events in early August (Figure 2b). The absorption by phytoplankton and reflectance ratio does not covary during the summer (Figure 2b). The reflectance at 640 nm, whose main source of variability is the backscattering coefficient, shows a peak in mid-June and a sustained minimum after 15 September (Figure 2c). The attenuation coefficient at 380 nm covaries well with the measured absorption by CDOM at 400 nm from the discrete samples (Figure 2d). The reason for the absence of covariation between the reflectance ratio and phytoplankton absorption becomes apparent when comparing the reflectance ratio (Figure 2b) with $K_d(380)$ (Figure 2d), which shows a strong covariance for the two measurements suggesting that the main factor influencing both measurements is the same, i.e., CDOM absorption. This strong effect of CDOM on the reflectance ratio has prevented us from developing a robust algorithm for phytoplankton biomass using the blue-green bands in these waters. In fact, even a standard inversion model [*Roesler and Perry*, 1995], which should in principle account for the influence of CDOM absorption on reflectance, has not allowed us to remove sufficiently its effect on the retrieval of phytoplankton biomass; small errors in the retrieval of CDOM cause large relative errors in phytoplankton absorption (results not shown). These errors are compounded by CDOM fluorescence.

[52] We first examine in more detail the IOPs measured and their variability in Lunenburg Bay. Secondly, we obtain a function describing the dependence of the quantum yield of fluorescence on irradiance. Thirdly, we test the new inverse model and closely examine the model results. Finally, we validate the model on an independent data set.

4.1. IOPs in Lunenburg Bay

4.1.1. Samples From Discrete Depths

[53] During the summer of 2003 in Lunenburg Bay, phytoplankton absorption at 490 nm varied between 0.02 and 0.06 m^{-1} with two spectra at approximately 0.08 m^{-1} (Figure 3a). This represents a very limited range of variability; in the NOMAD data set (version 1.3_2005262 [see *Werdell and Bailey*, 2005]) used for the development of satellite algorithms, phytoplankton absorption (calculated as total particulate absorption minus detritus absorption)
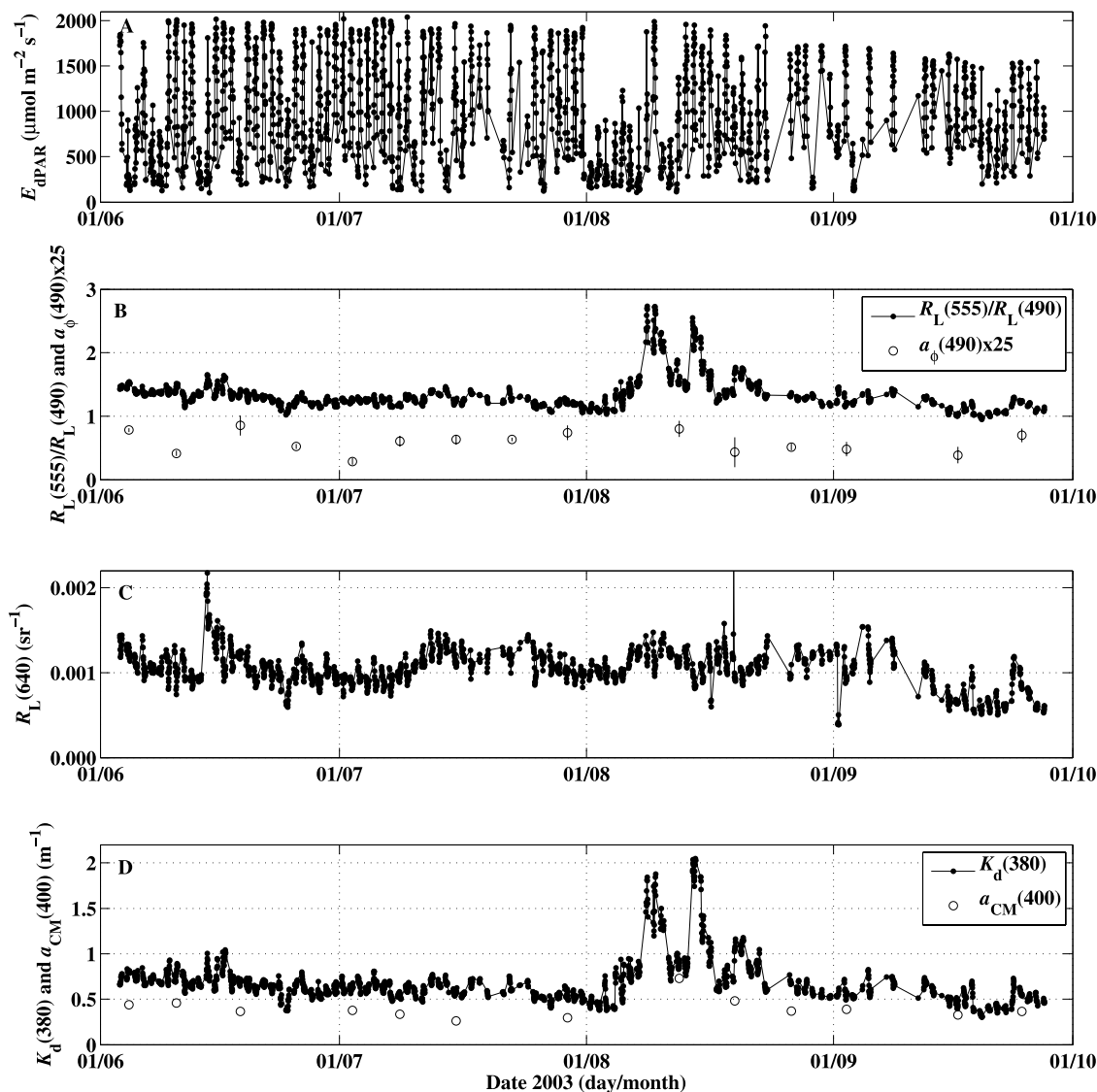
Figure 2. High frequency measurements from the MB1 optical mooring located in Lunenburg Bay, Nova Scotia, Canada, and discrete samples collected during weekly sampling at the mooring site. (a) Downwelling incident irradiance in the PAR waveband. (b) Radiance reflectance ratio at 555 and 443 nm measured with the hyperspectral TSRB and phytoplankton absorption measured near the surface during the weekly sampling. (c) Radiance reflectance at 640 nm measured with the hyperspectral TSRB. (d) Diffuse attenuation coefficient at 380 nm computed from the above surface irradiance sensor and a sensor located at 2.58 m, and absorption by the sum of nonalgal colored matter and CDOM at 400 nm.

ranges from 0.00065 to 1.02 m^{-1}. In our study, except for a few spectra that showed higher absorption at wavebands shorter than 450 nm, there was little variability in the shape of the phytoplankton absorption spectra (Figure 3b). The nonalgal particulate absorption varied between 0.025 and 0.25 m^{-1} at 400 nm (Figure 3c); however, the shape showed little variability (Figure 3d). The CDOM absorption was the largest fraction of the total absorption varying between 0.2 and 0.9 m^{-1} at 400 nm (Figure 3e), but once again the shape remained relatively stable over the whole summer (Figure 3f). The stability of the spectral shapes allowed us to use the mean spectra measured as constant shapes to represent the two absorbing components in the model:

(i) phytoplankton absorption and (ii) the sum of CDOM and nonalgal particulate absorption.

[54] The scattering coefficient (b, m^{-1}) measured with the ac-9 showed relatively flat spectra (Figure 4a), some of which featured a small spectral signature likely associated with phytoplankton absorption [see *Babin et al.*, 2003]. The backscattering coefficient showed a small decrease with wavelength for most spectra and varied for the most part between 0.004 and 0.01 m^{-1} with four spectra above 0.01 m^{-1} (Figure 4b). The backscattering ratio (b_b/b) also exhibited a slight decrease with wavelength (Figure 4c). The average value at 620 nm was 0.0144 with values mostly between 0.012 and 0.02; the mean value was used for all
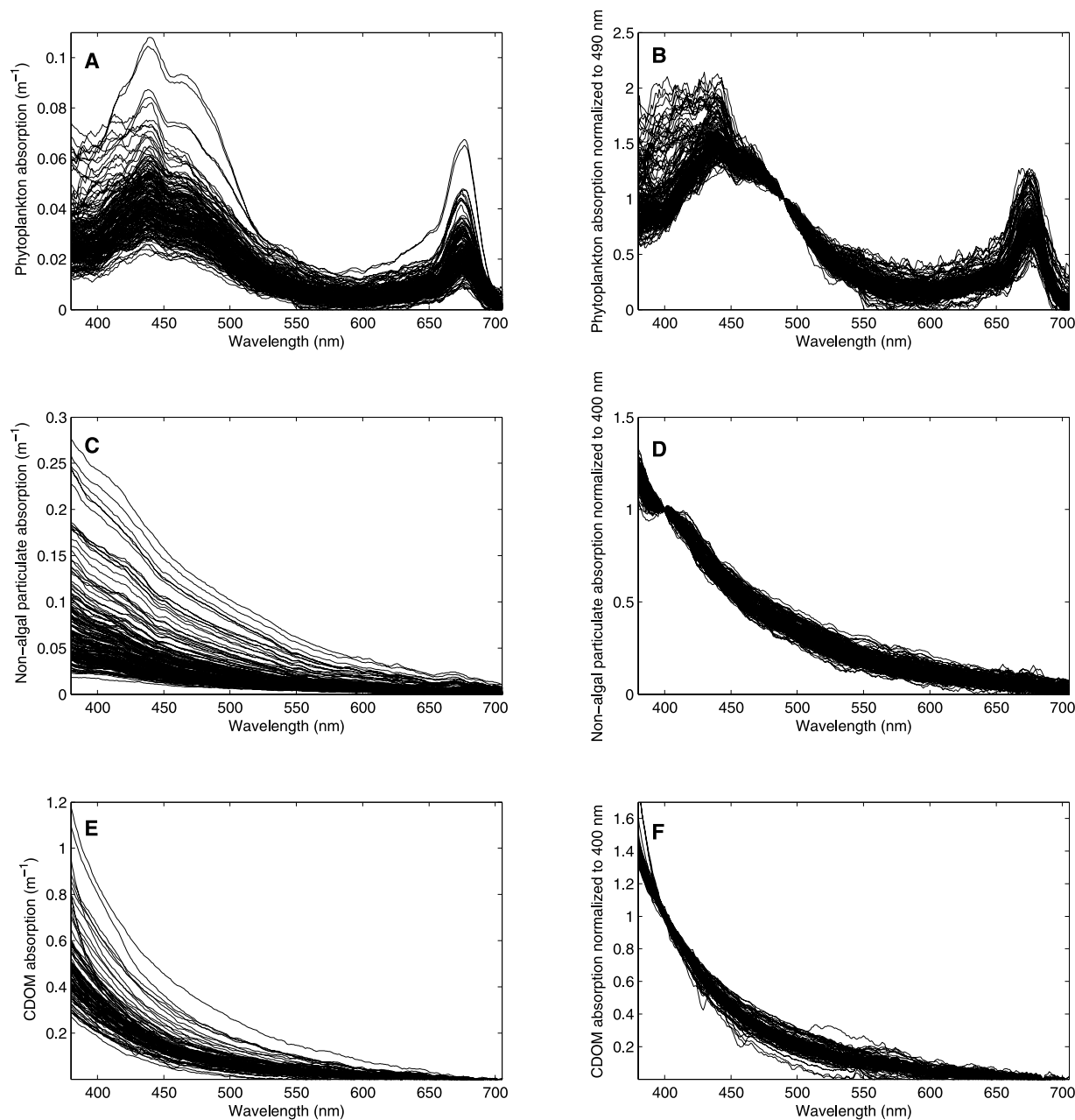
Figure 3. Absorption by phytoplankton, nonalgal particulate matter and CDOM measured in Lunenburg Bay during the summer of 2003. (a) Phytoplankton absorption, (b) phytoplankton absorption normalized to 490 nm, (c) nonalgal particulate matter absorption, (d) nonalgal particulate matter absorption normalized to 400 nm, (e) CDOM absorption, and (f) CDOM absorption normalized to 400 nm.

Hydrolight simulations and was assumed independent of wavelength.

4.1.2. Profiles and Observation Strategy

[55] Lunenburg Bay is usually stratified in summer and the optical properties vary with depth (Figure 5), the surface layer being more absorbing and scattering than the lower layers. At the near UV and red wavebands used for the inversion (see Table 2) absorption tends to be above 0.3 m^{-1}. Since 90% of the reflectance originates in the upper optical depth below the sensor [*Gordon and McCluney*, 1975], at the wavelengths used, assuming $K_d \sim a$, the upwelling radiance measured at 0.65 m originates above ≤ 3.65 m. The downwelling irradiance sensor was at a depth of ~2.5 m: this means that the reflectance and attenuation measurements were observing similar water layers. This would not be true for less attenuating wavebands where reflectance would effectively sample much deeper.

4.2. Fluorescence Spectral Components

[56] We compared the fluorescence emission spectrum of a neritic diatom, measured in this study, with spectra used by others (Figure 6). Note the large difference between the spectrum used by *Gordon* [1979], which is commonly used
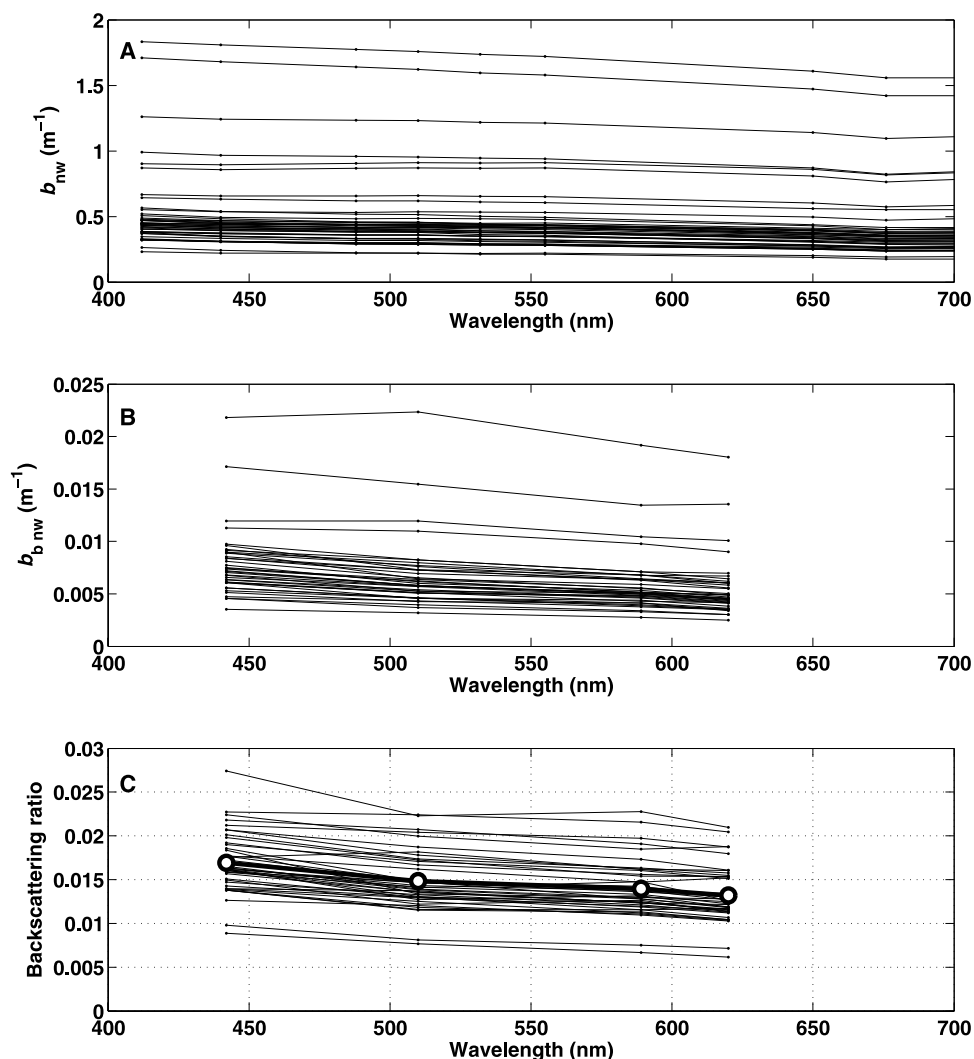
Figure 4. Spectral scattering, backscattering and backscattering ratio of particles measured in Lunenburg Bay in the summer of 2003. Spectra are averages for the top 5 m of vertical profiles: (a) Scattering coefficient measured with the ac-9, (b) backscattering coefficient, measured with the Hydroscat-6, and (c) backscattering efficiency, calculated as $b_{\mathrm{bnw}}/b_{\mathrm{nw}}$, (computed before depth averaging). The mean backscattering efficiency spectrum is plotted using white circles and a thicker line.

today [e.g., *Morrison*, 2003] and also used in the standard Hydrolight software, to simulate fluorescence emission in the ocean, and the measured spectra — a factor of about 2 at the longer wavelengths. The spectrum used by *Ostrowska et al.* [2000b], based on the Stokes shift of the red chlorophyll *a* absorption band, is much more similar to the measured spectra but lacks the ''secondary emission'' bands at the longer wavelengths (differences increase above ∼695 nm) originating from different chlorophyll-protein complexes [e.g., *Trissl*, 2003]. In our preliminary tests with the inverse model, the fits achieved with the *T. pseudonana* spectrum showed smaller and more randomly distributed residuals spectrally than those using the other spectra so we decided to use it for further model development.

4.3. Irradiance Dependence of the Quantum Yield of Fluorescence

[57] Before fluorescence can be used to accurately retrieve phytoplankton biomass under varying irradiance conditions, the change in the quantum yield with irradiance has to be accounted for. The reflectance measurements for the four-month deployment of mooring MB1 during the summer of 2003 were first inverted by keeping the quantum yield constant and independent of irradiance. When the quantum yield is held constant — here we chose a realistic value of 0.01 — variability in the retrieved absorption by phytoplankton is the result of: the real variability in absorption; variation in the quantum yield (due to changes in light intensity, physiology, species composition, or diurnal changes uncorrelated with irradiance); and random errors between the model and fit. Because absorption is not expected to vary directly with irradiance, we assume that the fraction of the variability explained by irradiance must originate from changes in the quantum yield of fluorescence. The apparent irradiance-dependence of phytoplankton absorption was fit to a linear model (Figure 7) using the modeled scalar irradiance weighted by the normalized phytoplankton absorption
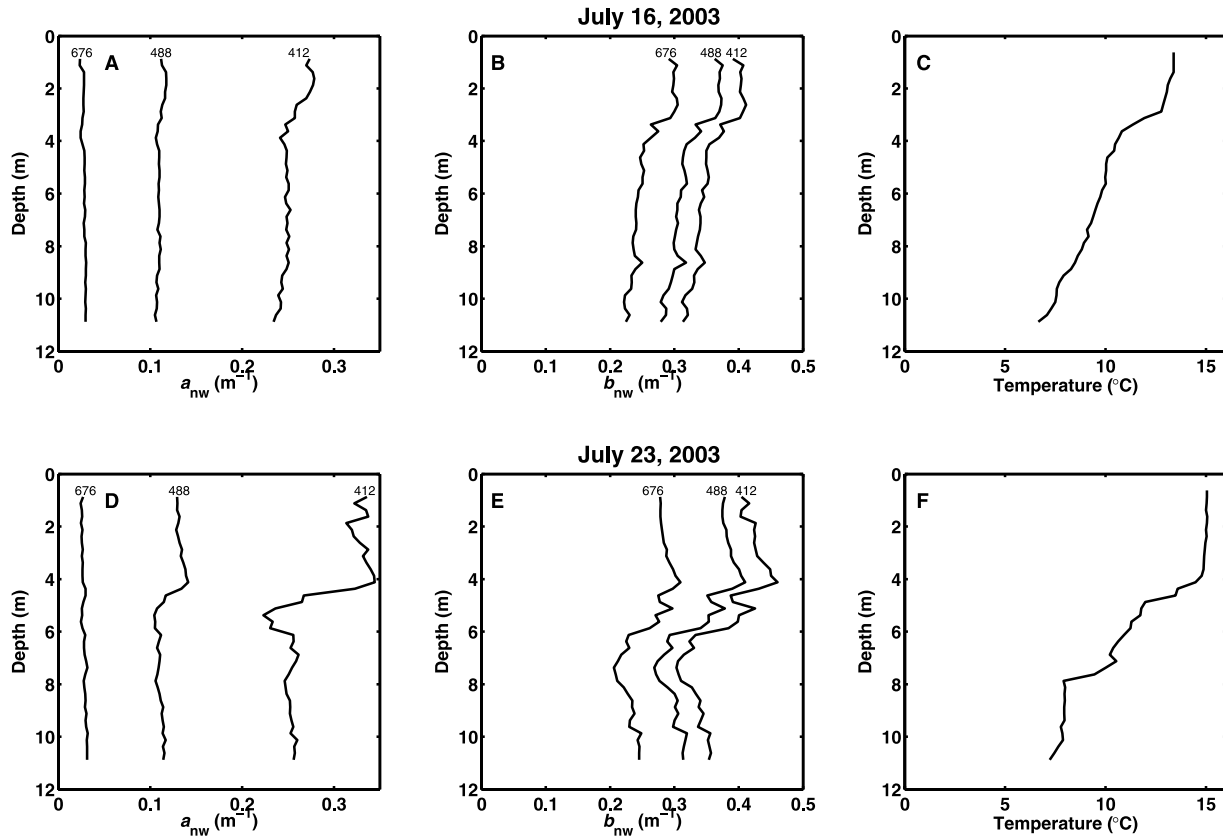
Figure 5. Profiles of absorption (a_{nw}, m^{-1}), scattering (b_{nw}, m^{-1}), and temperature (°C) for two days (top row is 16 July and bottom row is 23 July) during the summer of 2003. The absorption and scattering are for particulate plus dissolved matter at 412, 488 and 676 nm as labeled above the respective lines.

spectrum (photosynthetically utilizable radiation, PUR) at 0.65 m (E_{PUR}^{490} (0.65)) as the independent variable,

$$E_{PUR}^{490}(0.65) = \int_{400}^{700} \bar{a}_{\phi}^{490}(\lambda) \overset{o}{E}(\lambda, 0.65)d\lambda, \qquad (16)$$

where $\bar{a}_{\phi}^{490}(\lambda)$ is the phytoplankton absorption coefficient normalized to its value at 490 nm and $\overset{o}{E}(\lambda, 0.65)$ is obtained using $E_d(\lambda_{ex}, 0^+)\overset{o}{\mathbf{T}}{}^{mod}|_{0+}^{0.65}$. Our definition of PUR uses absorption normalized to 490 nm, rather than to the maximum [*Morel*, 1978] or the mean absorption [e.g., *Markager and Vincent*, 2001], since the phytoplankton spectral shape was normalized to 490 nm for modeling; the formulation has no significant influence on the results. The PUR was used for this analysis as it was the best proxy that could be obtained for the exciting radiation for phytoplankton fluorescence (the ideal weighting would be the fluorescence excitation spectrum). The fitted relationship for the retrieved phytoplankton absorption versus irradiance as a function of E_{PUR}^{490} for all four months (Figure 7), denoted $a_{\phi}^{yield}(E_{PUR}^{490})$ (m^{-1}), can be used to describe the irradiance dependence of the quantum yield of fluorescence (see equation in Figure 7). However, this relationship provides only the relative irradiance dependence, and the absolute value of the quantum yield, which would scale this relationship, can only be obtained through

validation with in situ phytoplankton absorption data (see section 4.4.1).

4.4. Verification With the 2003 Data

[58] The first test of the model consists of analyzing the reflectance spectra and attenuation coefficients measured by the optical mooring at the time of collection of the discrete samples for 2003. The reflectance spectra show limited variability (Figure 8), but two spectra are clearly different; one from 13 August, which shows lower reflectance in the UV-blue region consistent with larger than usual CDOM absorption (also see Figure 2d), and one from 17 September showing lower reflectance in the 600–650 nm region, consistent with a lower than average backscattering coefficient (also see Figure 2c).

4.4.1. Phytoplankton Absorption and Scaling the Quantum Yield Versus Irradiance Relationship

[59] After inversion of the selected spectra presented in Figure 8, we obtained the IOPs associated with each spectrum, which can be compared with the in situ samples (Figure 9). This comparison shows that phytoplankton absorption is well retrieved, despite the limited variability observed (Figure 9a).

[60] To obtain this graph, and all inversions thereafter, the quantum yield of fluorescence used during the inversion was specified as a function of incident irradiance consistent with the irradiance-dependence of the quantum yield (a_{ϕ}^{yield} (E_{PUR}^{490}) in Figure 7), scaled by a factor of 0.4 m such that the
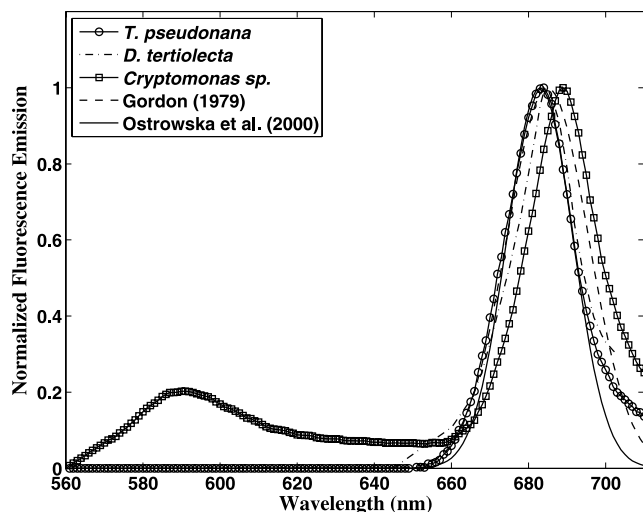
Figure 6. Five emission spectra for phytoplankton fluorescence normalized to their maximum values. The spectra are for *Thalassiosira pseudonana* (this study); *Dunaliella tertiolecta* [*Collins et al.*, 1985] (their "Sun" spectrum digitized and extrapolated in the short wavelengths); *Cryptomonas* sp. [*Sciandra et al.*, 2000] (extrapolated linearly in the short wavelengths); and two theoretical shapes from *Gordon* [1979] and *Ostrowska et al.* [2000a].
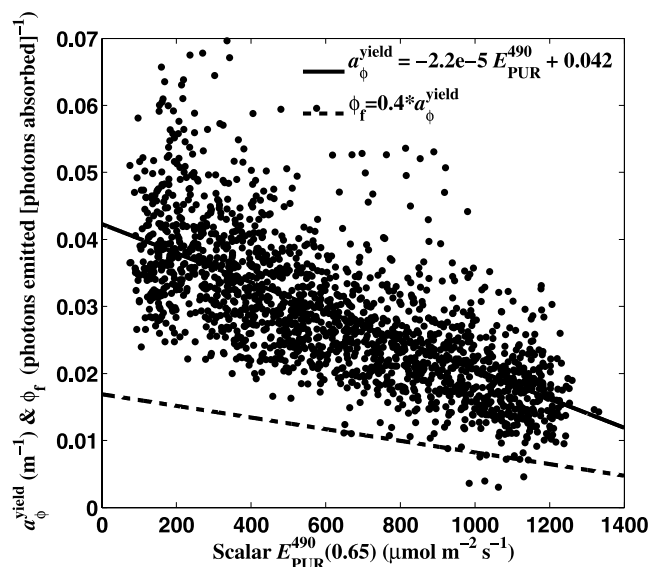
retrieved a_φ followed the 1:1 line in Figure 9a as closely as possible. The final relationship for the quantum yield used in equation (12) during the inversion is thus (shown in Figure 7): $\varphi_f(E_{PUR}^{490}) = -8.684 \times 10^{-6} E_{PUR}^{490} + 0.0169$. That is, at each iteration of the optimization routine, the value of $\varphi_f(E_{PUR}^{490})$ was used in equation (12) in place of φ_f. The most important effect of the scaling (within a reasonable range) is to translate all points vertically (Figure 9a), with little effect on the correlation coefficient. In this panel, errors in the estimation of phytoplankton absorption are typically within 25%, however, one point clearly stands out. This point corresponds to the sampling day of 17 September 2003. In addition to having a distinct reflectance spectrum, the HPLC pigments obtained for that day from discrete samples show a large peak, probably corresponding to a phaeophytin (not fluorescing), which was not seen in any other samples that year (C. Normandeau, personal communication). Clearly, the optical and environmental conditions for that day were different from the rest of the season.

4.4.2. Absorption by Colored Matter and Backscattering

[61] Because $K_d(380)$ is fitted very well (see section 4.5 and Figure 10), and is mostly influenced by CDOM absorption in these waters, a strong relationship between the measured and retrieved absorption by nonalgal colored matter at 400 nm is expected. Indeed, retrieval of a_{CM}
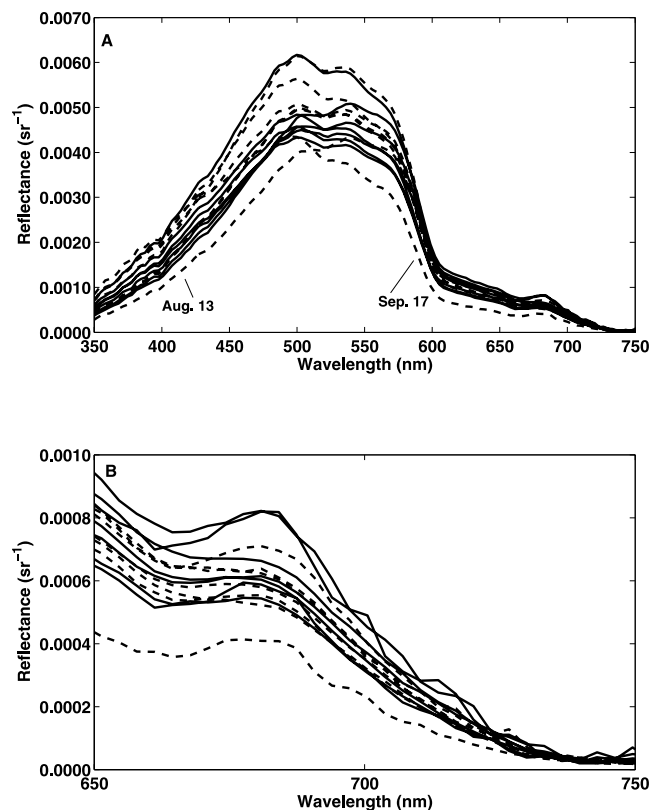

Figure 7. Regression of the retrieved absorption coefficient for phytoplankton as a function of the scalar PUR irradiance at 0.65 m when the quantum yield of fluorescence is kept constant at 0.01 in the inverse model. Under these conditions, the variability observed originates from the natural variability of phytoplankton absorption and the natural variability in the quantum yield of fluorescence plus random errors. The dashed line is the quantum yield of fluorescence used in the model; it is obtained by multiplying the top line by 0.4 to obtain a relationship as close as possible to a 1:1 line in Figure 9a.

Figure 8. Reflectance spectra used for the inversion that have matching IOP spectra. Each spectrum was recorded immediately following the time at which the discrete samples were taken at station MB1 during the summer of 2003 in Lunenburg Bay. (a) Full spectra and (b) fluorescence spectral region only.
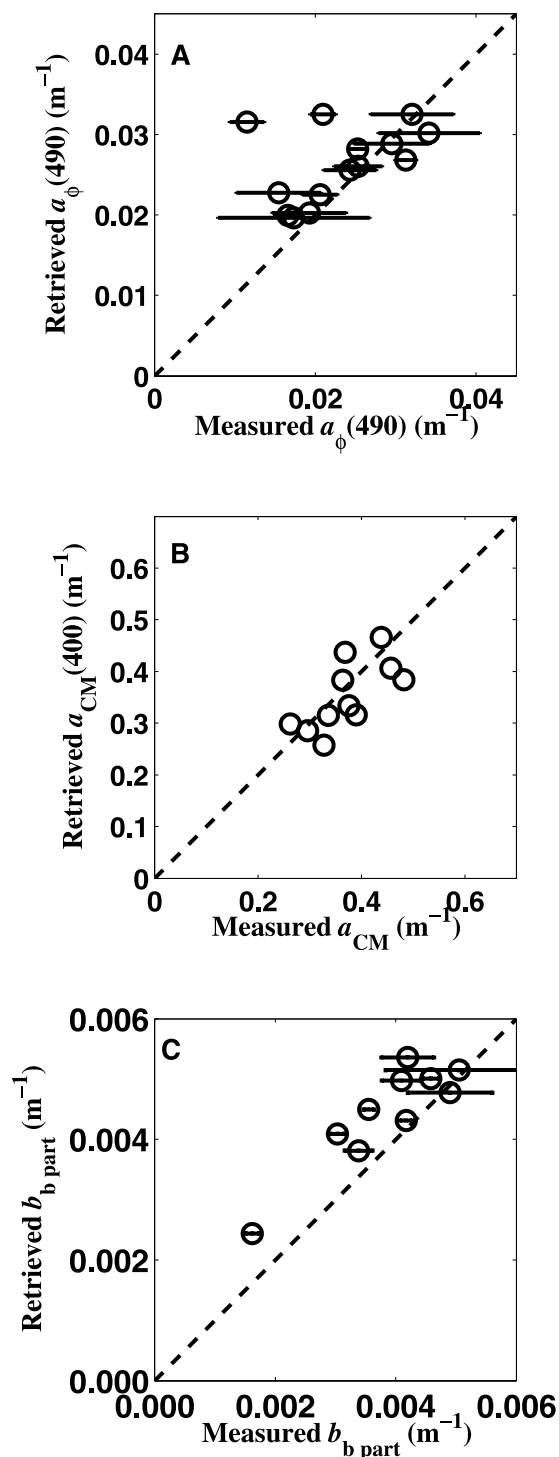
Figure 9. Comparison of the measured and retrieved absorption coefficients at the MB1 buoy during the summer of 2003. (a) Absorption by phytoplankton at 490 nm. Measured points are the mean of two samples collected at 1 m. Error bars represent the range. (b) Absorption by nonalgal colored matter. Points represent a single measurement at 1 m of CDOM plus detritus (absorption from the extracted samples of the phytoplankton filter). (c) Backscattering coefficient of particulate matter at 620 nm. Error bars correspond to the standard deviation of the Hydroscat-6 measurements of the over the first 5 m (~40 points). On all panels, the dashed black line is the 1:1 line.

follows the 1:1 line closely, and despite the limited variability observed for the measured samples, the model retrieved a significant fraction of this variability (Figure 9b, $r = 0.78$, $n = 12$, p = 0.003). Reasons for the unexplained variability include spatial heterogeneity (samples were usually collected within 50 to 100 m of the mooring), the delay between the water sampling and AOP measurements (usually less than an hour), and the difference between the integrated values obtained from the K_d measurement and the discrete samples obtained from the bottle.

[62] The trend in the backscattering coefficient at 620 nm (Figure 9c) is well retrieved given, again, the limited variability observed. There is, however, a consistent overestimate of backscattering by the model. The difference, however, is acceptable, given the fact that both the Hydroscat-6 and the model provide indirect estimates of the backscattering coefficient.

4.5. Inversion Results for Eight Consecutive Days

[63] To allow us to inspect the ability of the model to capture diel variability, we analyze the model output for eight days in August 2003 (Figure 10). A comparison of the retrieved attenuation coefficient at 380 nm (i.e., the value of the LUT for $\mathbf{K}_d^{mod}(\lambda)|_{0+}^{2.75}$ when the IOPs retrieved from the inversion are used) with the attenuation coefficient measured by the irradiance sensor at the surface and at z_{Ed} is shown in Figure 10a. Since attenuation at 380 nm is one of the inputs to the optimization (see Table 2 and Figure 1) comparing the retrieved attenuation with the measurement at this wavelength is mostly a measure of the goodness of fit. The figure shows that the measured and retrieved attenuation coefficients are essentially identical; the modeled points are all superimposed on the measurements, implying that the fit at this waveband is very good. The K_d at 490 nm is not used during the optimization and, since K_d is mostly influenced in these waters by absorption, a comparison of the retrieved values for $\mathbf{K}_d^{mod}(490)|_{0+}^{2.75}$ with the measurements can be used as a measure of the quality of the retrieval of absorption at that wavelength. However, because $K_d(490)$ is mostly influenced by CDOM and nonalgal colored matter (the influence of phytoplankton absorption on K_d is illustrated in Figure 12b), and considering that $K_d(380)$ is almost perfectly fit, it is mostly a test showing that the shape of absorption by colored matter used in the model is appropriate and the spectral model for K_d is accurate.

[64] On the same panel (Figure 10a), the retrieved and measured absorption by colored matter, $a_{CM}(400)$ are shown. This section of the time series coincides with a heavy rain event in the region, which led to increased runoff from land and a steep increase in CDOM absorption. This absorption subsided within three days to return to values similar to those observed before the event. The rain event also led to a modest increase in the phytoplankton concentration (Figure 10b), as retrieved by the model. For this period, the inversion retrieves phytoplankton absorption within the error bars of the measurements.

[65] The retrieved backscattering coefficient by particles at 620 nm ($b_b(620)$, Figure 10c) did not show any change with the increase in CDOM absorption but did show some diel variations. This variability could be natural or an artifact of the parameterization of the LUT (e.g., an incor-
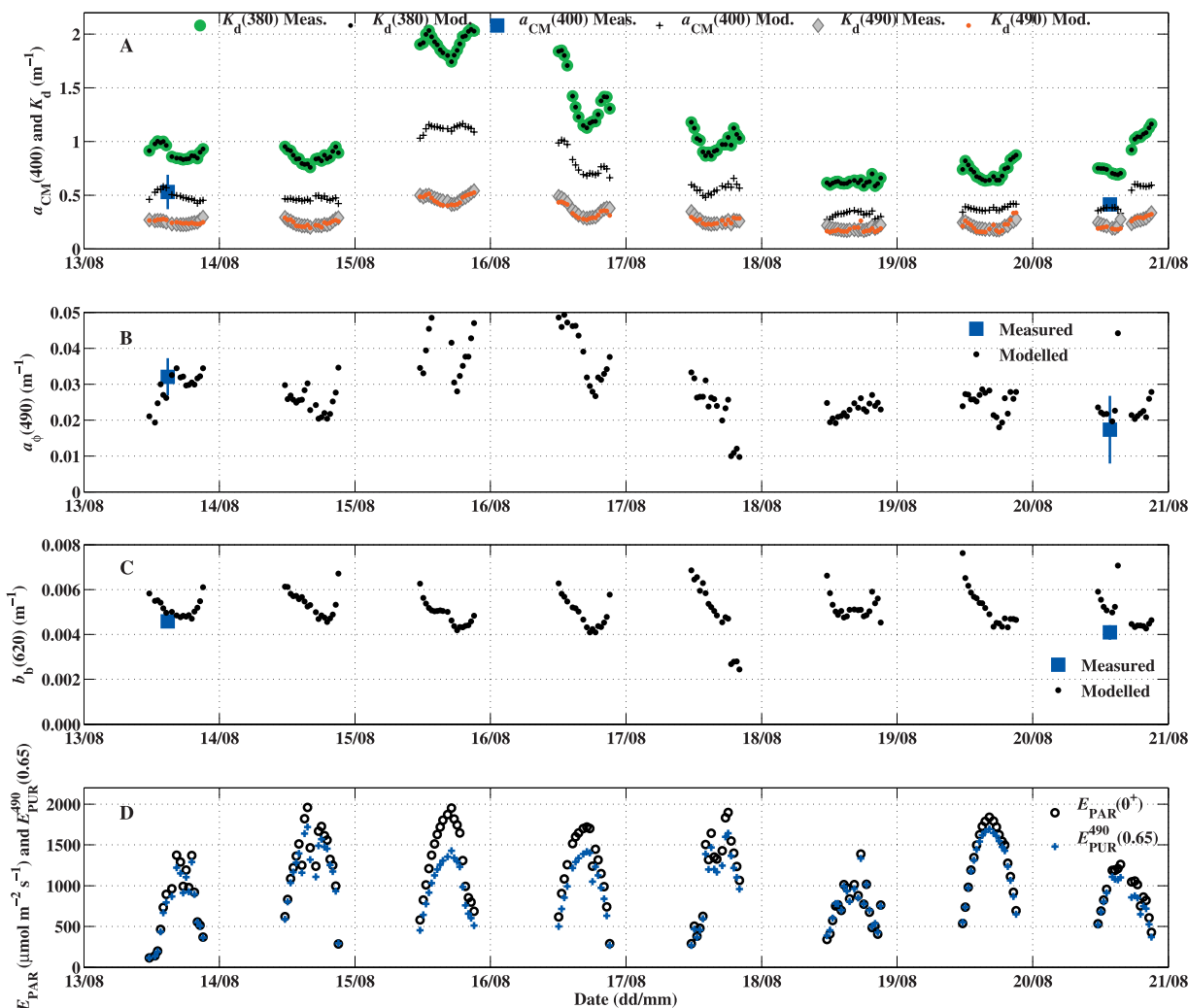
Figure 10. Time series comparison of the in situ optical measurements and their retrieval with the inverse model. (a) Measured and retrieved absorption by nonalgal colored matter (at 400 nm) and the diffuse attenuation coefficient at 380 and 490 nm. Squares are absorption by colored matter measured with a spectrophotometer. Points for the modeled $K_d(490)$ are always beneath the measured points. (b) Measured and retrieved absorption coefficient for phytoplankton. Phytoplankton absorption was measured using the filter pad method (see Figure 9 for error bar definition). (c) Particulate backscattering coefficient retrieved from the inversion and measured using a Hydroscat-6, both at 620 nm. (d) Measured incident planar irradiance in the PAR domain and modeled scalar PUR at 0.65 m. The PUR irradiance has been normalized to the first point (13/08) of the PAR irradiance to allow assessment of the effect of variable colored matter absorption on the ratio of PAR above the surface to PUR at 0.65 m.

rect angular shape of the volume scattering function); however, we do not have diel time series from the Hydroscat-6 to verify the presence or absence of this variability in situ. For this time period, the retrieved backscattering coefficient of particles compares well with the measurements made using the Hydroscat-6 instrument despite slightly higher retrieved values.

4.5.1. Measures of Fluorescence Excitation Irradiance

[66] Different excitation irradiances can be used when modeling the effect of irradiance on the quantum yield of fluorescence. The ideal measure would be the irradiance absorbed by photosynthetic pigments associated with photosystem II [e.g., *Huot et al.*, 2005, Appendix II; *Sosik and Mitchell*, 1995]. Since we did not have this information, we chose to use the irradiance weighted by total phytoplankton absorption. A comparison of $E_{dPAR}(0^+)$, a metric used in previous studies, and $E_{PUR}^{490}(0.65)$ shows that their ratio is variable (Figure 10d, see also Figure 11). To allow a comparison of the differences between the two measurements, the value of the $E_{PUR}^{490}(0.65)$ time series is scaled such that the value of the first point is the same as the first point of the $E_{dPAR}(0^+)$ time series (see equation (12)). If $E_{dPAR}(0^+)$ was used instead of $E_{PUR}^{490}(0.65)$, the variability observed in the ratio would lead to 25 to 30% errors in the retrieval of phytoplankton absorption using fluorescence (Figure 10d). The two main sources of variability in the ratio $E_{PUR}^{490}(0.65)/E_{dPAR}(0^+)$ are the attenuation coefficient and the solar zenith angle, the former being more important over the
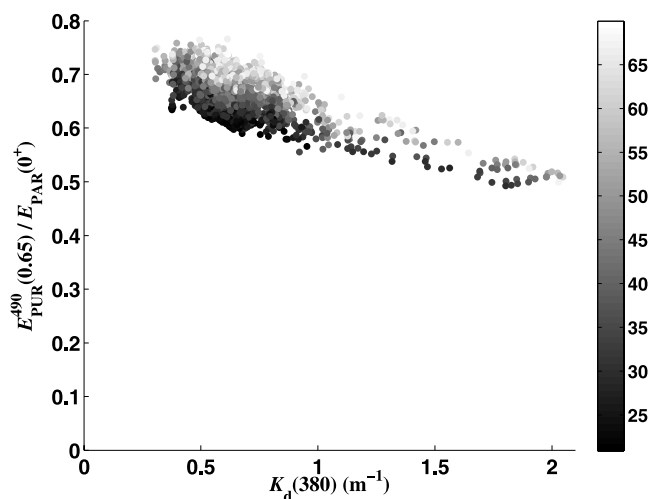
Figure 11. Variability of the ratio $E_{PUR}^{490}(0.65)/E_{PAR}(0^+)$ as a function of the diffuse attenuation coefficient at 380 nm. Points are shaded according to the zenith Sun angle (degrees).

whole season in Lunenburg Bay (Figure 11). Thus, while $E_{dPAR}(0^+)$ is a good approximation of the excitation irradiance in some cases, we found that in highly attenuating and optically variable waters, and when the upwelling radiance sensor is not just below or above the surface, a PUR-weighted irradiance is necessary for accurate results.

4.5.2. Effect of the Solar Zenith Angle on the Retrieval of the Absorption Coefficients

[67] A closer inspection of Figure 10a reveals the benefit of accounting for the effect of the solar zenith angle in the look-up table on a sunny day and the erroneous influence it can have on a retrieval for a cloudy day. On 15 August (also see 14 and 19 August), the $K_d(380)$ and $K_d(490)$ measurements show a decrease around midday consistent with a smaller solar zenith angle [e.g., *Zheng et al.*, 2002] and a reduced average path length for photons in the water (and decreased surface reflection). The retrieved absorption coefficient by colored matter at 400 nm (a_{CM}, Figure 10a), as expected, shows no or little effect related to the solar angle. On 18 August, which was obviously overcast (see Figure 10d), the measurement of $K_d(380)$ remained constant through the day, which is not surprising given the unchanging angular distribution of a diffuse light field (and unchanging water mass), but the retrieved absorption by colored matter at 380 nm showed a maximum at noon since the look-up table is over-correcting for the effect of the solar angle.

4.6. Examining the Fit on One Spectrum

[68] We now focus on one representative spectrum for which matching in situ data is available in order to examine more closely our choice of wavebands for the inversion.

4.6.1. The 400 to 600 nm Wavebands

[69] The comparison between the retrieved and measured spectra for 16 July 2003 shows a striking lack of fit for the reflectance spectra between 400 and 600 nm with obvious nonrandom residuals in this region (Figure 12a). The attenuation coefficient is, however, well retrieved over the

whole spectrum from 380 to 555 nm (Figure 12b, with some error at 555 nm), suggesting that the retrieval of the total absorption (also decomposed into its different constituents in the figure) is good at least up to 500 nm. Comparison of the backscattering spectrum (Figure 12c) obtained during the inversion with the measured spectrum shows consistent spectral values and amplitudes, at least as much as can be expected from these two indirect measures. The good fit in the wavebands used for the optimization along with the
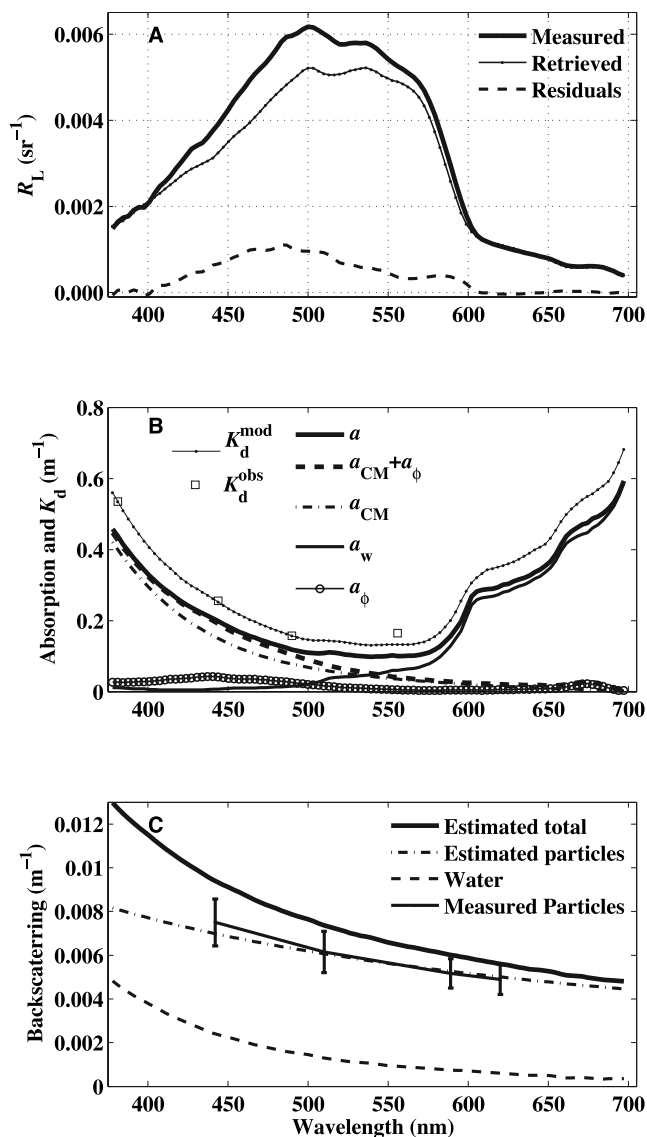

Figure 12. An example run of the inverse model on 16 July 2003 (see Figure 5a). (a) The measured and retrieved spectra of radiance reflectance and residuals. The fitted wavebands show low residuals, while high and positive residuals are found between 400 and 600 nm. (b) Modeled diffuse attenuation, K_d^{mod}, observed diffuse attenuation, K_d^{obs}, and retrieved absorption coefficients. Only the waveband at 380 nm is fitted for K_d, but all four are modeled. (c) Fitted and measured backscattering coefficient. Error bars on the backscattering coefficient represent the standard deviation of the measurement between 0 and 5 m (n ≈ 30).
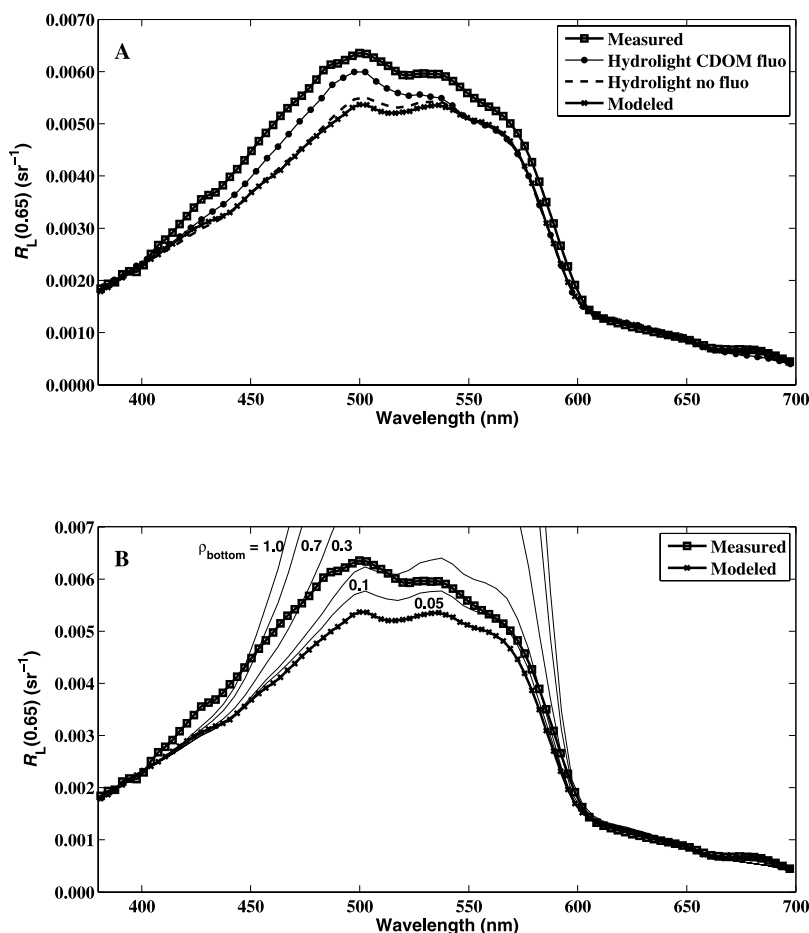
Figure 13. Comparison of the measured and fitted spectra with Hydrolight simulations. (a) Effect of CDOM fluorescence. The Hydrolight spectrum without fluorescence (mostly underneath the modeled spectrum) was obtained by inserting the IOPs retrieved by the inversion into Hydrolight (otherwise keeping the same parameterization as for the LUT). (b) Effect of bottom reflectance. The Hydrolight simulations were carried out without CDOM fluorescence but using different bottom reflectances (ρ_{bottom}), keeping the water depth constant at 13 m. For both panels, the measured spectra have been corrected for shading to compare with the Hydrolight simulations (Appendix B). The measured and fitted spectra are the same as those shown on Figure 12 and the profiles of Figure 5 for 16 July.

good retrieval of absorption and backscattering for this spectrum lead us to believe that the differences observed between the measured and retrieved reflectance spectra (Figure 12a) are real and result from processes that are not taken into account in the model but are present in the environment. Below we examine two possible processes.

4.6.2. Effects of CDOM Fluorescence and Bottom Reflectance in Lunenburg Bay

[70] Ignoring Raman scattering, which would not produce the spectral shape observed above for the residuals, there are two terms in equation (2) that are not included during the inversion: CDOM fluorescence and bottom reflectance. To test the potential impact of these two terms on the upwelling radiance at the MB1 site, we inserted the IOPs retrieved from the inverse model into Hydrolight using the same parameters that were used during the LUT parameterization along with the solar angle appropriate for the time of measurement. We computed the reflectance spectra expected for an infinitely deep water column without bottom reflectance for two scenarios: one without CDOM

fluorescence and a second with CDOM fluorescence included (with the standard Hydrolight fluorescence redistribution function, Figure 13a). We also did the computation using a spectrally neutral bottom reflectance of 0.05, 0.1, 0.3, 0.7, and 1.0, a bottom depth of 13 m, without CDOM fluorescence (Figure 13b). These comparisons are limited in the sense that we do not have any information for Lunenburg Bay concerning the variable spectral redistribution function for CDOM fluorescence or the spectral bidirectional reflectance of the bottom. But the comparisons do provide a first order test of their possible impacts and suggest that both CDOM fluorescence and bottom reflectance could contribute to the differences observed in Figure 12a. Clearly, bottom reflectance could explain most of the differences observed between ~440 and 600 nm, but the orange "edge" around 600 nm imposes a strict limit on the amplitude of the bottom reflectance, suggesting that it is not much greater than 0.05 in this region. Even if the spectral shape of bottom reflectance increased strongly at the short wavelengths (it cannot be greater than 1.0), this

leaves a band between 400 and ~530 nm, which requires CDOM fluorescence to account for the difference. Thus we suspect that Lunenburg Bay CDOM is characterized by a slightly broader CDOM redistribution function than the one used for the Hydrolight simulation, which would contribute by filling in the remaining gap in reflectance (mostly between ~410 and 450 nm). To go beyond this simple hypothesis requires in situ information about the substrate's bidirectional reflectance function and the CDOM fluorescence spectral redistribution function.

4.7. Validation of the Retrieved Phytoplankton Biomass Using the 2004 Data

[71] For this validation, we use the sum of chlorophyll plus phaeopigment data collected at three mooring sites in the summer of 2004 (Figure 14). The model retrieves the absorption coefficient for phytoplankton at 490 nm using fluorescence. This product is compared with the chlorophyll plus phaeopigments measured in situ (Figure 14a) and the correlation coefficient is $r = 0.76$ (n = 93, p = $\ll 0.001$) with a mean absolute percentage error (mean of | Estimated - Measured |/Measured, MAPE) of 24%. The modeled absorption value can be transformed directly into a chlorophyll concentration using a simple linear relationship (Figure 14b).

[72] Our model was developed for optically complex Case 2 waters in which CDOM dominates absorption. It is interesting to compare our model results to those obtained from a global data set of chlorophyll concentration for optically simpler Case 1 waters and standard ocean color algorithms used in those waters. This comparison is shown in Figure 14c using the NOMAD data set [*Werdell and Bailey*, 2005], which is the data set used for algorithm development for the NASA ocean color sensors. For this comparison, we used only the chlorophyll data obtained by HPLC and, significantly, we restricted the range of chlorophyll concentration to that measured in Lunenburg Bay. The OC4V4 [*O'Reilly et al.*, 1998] algorithm retrieves chlorophyll for this data set with a correlation coefficient of $r = 0.67$ (n = 384, MAPE = 52%). Thus, our local algorithm (r = 0.76, MAPE = 24%), using Sun-induced fluorescence in Case 2 waters, where conventional algorithms do not work retrieves chlorophyll as well as, or more accurately, than a state-of-the-art ocean color algorithm applied for Case 1 waters on a global data set, when restricted to the same range of chlorophyll concentrations.

5. Discussion

[73] The inverse model of ocean color developed here allows for the estimation of phytoplankton biomass in
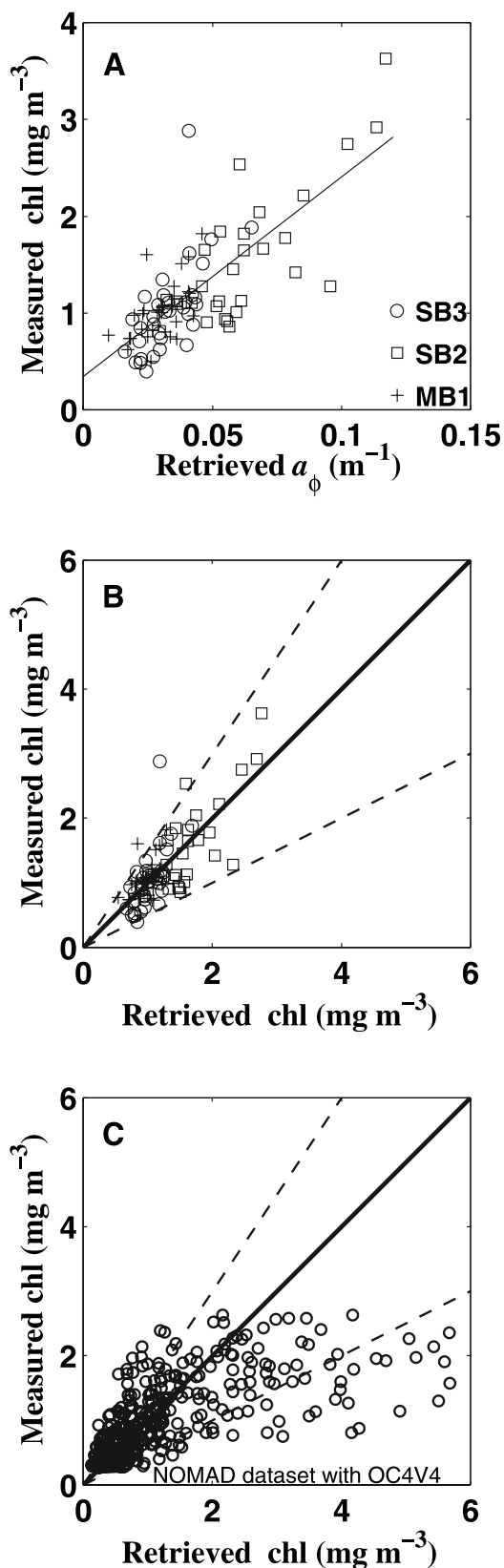

Figure 14. Comparison of retrieved and measured phytoplankton biomass. (a) The retrieved absorption coefficient at 490 nm obtained directly from the inversion is compared with the measured chlorophyll plus phaeopigments concentration for all three moorings during the summer of 2004. The line corresponds to the best fit line. (b) Chlorophyll estimated from the best fit line from Figure 14a compared with the measured chlorophyll. The dashed lines represent the 50% error boundary from the 1:1 line. (c) For comparison, the retrieval of chlorophyll concentration from the NOMAD data set using the OC4V4 chlorophyll algorithm used with the SeaWiFs sensor. The NOMAD data set is composed in large part of the data set used for the construction of the OC4V4 algorithm.

coastal waters where the absorption signature of phytoplankton is masked by CDOM absorption. Three key aspects of the model are: the simultaneous inversion of the diffuse attenuation coefficient and reflectance using look-up tables; the use of Sun-induced fluorescence; and the omission of wavebands from 400 to 605 nm. We first discuss these three aspects before comparing our algorithms with those of others, who also use Sun-induced fluorescence to retrieve phytoplankton biomass.

5.1. Simultaneous Inversion of Two AOPs

[74] The simultaneous inversion of reflectance and the diffuse attenuation coefficient, albeit with different approaches, has been previously attempted [*Gordon*, 1974; *Loisel and Stramski*, 2000; *Loisel et al.*, 2001]. *Gordon* [1974] used the product of the two to retrieve a proxy of the backscattering coefficient. Using this method, Gordon first discovered the spectral signature of fluorescence in a spectrum from the San Vicente Reservoir. He misidentified it at the time as being the result of anomalous dispersion from chlorophyll *a* absorption, but later correctly identified and modeled the peak in a seminal paper on Sun-induced fluorescence [*Gordon*, 1979]. Using semiempirical relationships derived from radiative transfer simulations, *Loisel and Stramski* [2000] and *Loisel et al.* [2001] inverted reflectance and K_d to retrieve the absorption, scattering and backscattering coefficients. They did not, however, attempt to retrieve phytoplankton absorption.

[75] Our goal is different from these two studies in that we intend to retrieve phytoplankton biomass in coastal waters using Sun-induced fluorescence and eventually to include these estimates in an ecosystem model of the bay. The main objective of the inversion of the elastic component is thus to provide the appropriate parameters and representation of the AOPs for the simultaneous use of a Sun-induced fluorescence model (equation (12)); retrieving the IOPs is a useful, but, in this case, secondary outcome. Our approach is also slightly different from the other inversion models in that we did not attempt to formulate semiempirical relationships, but instead used LUTs to represent the AOPs. The use of LUTs simply allowed for more versatility in the relationships needed for our group of sensors. This came at a cost, however, as in its present implementation this method is significantly slower than using a simple semianalytical method (a previous version of the model based on such relationships was used by *Huot* [2004]), as several multivariate interpolations have to be carried out on four look-up tables at each iteration of the optimization routine. *Wang et al.* [2005], using a hyperspectral TSRB without the K_d component, described the forward model used in their inversion by an analytical function. As such, they accounted analytically for the geometry of the instrument. This allowed them to use a very fast optimization scheme and to provide error estimates on the retrieved values. In their study, however, the parameters used in the functions describing the relationships between IOPs and AOPs are not spectrally dependent and the fluorescence band is not taken into account.

5.2. Sun-Induced Fluorescence Model

[76] The model used in this study to describe the upwelling fluorescence radiance is very similar to robust models

developed by others [e.g., *Maritorena et al.*, 2000; *Morrison*, 2003; *Ostrowska et al.*, 1997], though its inclusion directly within an inverse model to retrieve estimates of phytoplankton absorption and chlorophyll concentration is new. Accurate retrieval of phytoplankton absorption should not depend on the form of the fluorescence model used, but instead on a good retrieval of spectral K_d and limited variability in the quantum yield of fluorescence in surface waters. While the accurate retrieval of K_d was verified with in situ measurements of K_d, the limited variability in the quantum yield was verified ultimately by comparing the retrieved and measured biomass.

[77] To reduce unexplained variability in the quantum yield of fluorescence, we describe it as a function of the incident irradiance. Although this approach has been advocated by *Cullen and Lewis* [1995] for active fluorescence (but rarely applied), and Sun-induced fluorescence yield has been described as a function of irradiance [e.g., *Morrison*, 2003], to the best of our knowledge, this is the first time such a dependence has been applied to the retrieval of phytoplankton biomass from natural fluorescence measurements. Without using this dependence, the model would predict an artifactual decrease in phytoplankton absorption in bright light. A similar bias is also observed in near-surface fluorescence profiles. The mean curve computed for the summer of 2003 (Figure 7) shows that the quantum yield of fluorescence varied by a factor of ~3 due to changes in irradiance; this is a considerable source of variability, as the whole range of irradiance can occur within one day. Thus, if it is not accounted for, within one day, the retrieved phytoplankton absorption could decrease by a factor of 3 as irradiance increases, independent of changes in biomass. In our data set, the biases due to changes in irradiance could be as large as the changes in biomass that were observed over the whole season during the weekly sampling (see Figure 9). It should be kept in mind, however, that the irradiance dependence described here may not be applicable to all environments.

[78] Similarly, because the incident PAR irradiance at the surface is not necessarily a good predictor of the PUR irradiance at 0.65 m (Figure 10d and Figure 11), an accurate description of the latter is essential otherwise errors on the order of 30% for phytoplankton absorption are unavoidable in highly attenuating waters (Figure 11). The same applies to regions where phytoplankton absorption is strong, since phytoplankton absorption, by definition, has a strong influence on changes in PUR with depth [*Markager and Vincent*, 2001].

[79] The attribution of all the irradiance dependence of a_ϕ^{yield} (Figure 7) to changes in the quantum yield is not necessarily correct; part of the variability could originate from diel changes in the absorption of phytoplankton [e.g., *Ohi et al.*, 2002; *Stramski and Reynolds*, 1993]. As such, attributing all the variability to the quantum yield could bias the retrieval of a_ϕ. For example, imagine a hypothetical situation where the quantum yield in situ remained constant and all the decrease observed in the fluorescence radiance with increased irradiance would be due to a decrease of phytoplankton absorption. Our erroneous attribution of the decrease in L_{uf} at midday to changes in the quantum yield would lead the model to erroneously predict constant phytoplankton absorption. However, the decrease of the

quantum yield of fluorescence at high irradiances is well documented as originating from photoprotective mechanisms that cause nonphotochemical quenching of fluorescence under high light [*Demers et al.*, 1991; *Falkowski and Kolber*, 1995; *Kiefer*, 1973; *Krause and Weis*, 1991; *Müller et al.*, 2001; *Ruban et al.*, 2004], while diel changes in absorption do not lead to the lowest values at the time of highest irradiance [e.g., *Ohi et al.*, 2002; *Stramski and Reynolds*, 1993].

5.3.   Omission of Wavebands

[80]   During development of this model, we spent considerable time trying to incorporate the wavebands from 400 to 605 nm, but the model showed significantly worse fits when using these wavebands. Our simulations for Lunenburg Bay (Figure 13) show that CDOM fluorescence could have a significant impact on the retrieval of phytoplankton absorption using the inverse model because CDOM fluorescence emission significantly increases reflectance in a spectral band that overlaps with the phytoplankton absorption band in the blue. The problem of CDOM fluorescence has been studied previously, and shown to be important in certain locations [e.g., *Pozdnyakov and Grassl*, 2003]. The unknown spectral redistribution function for Lunenburg Bay prevents us from modeling these effects in the inverse model.

[81]   Bottom reflection could also be incorporated into the inverse model; forward models that account for bottom reflectance exist [e.g., *Albert and Mobley*, 2003] and new look-up tables could be described. However, for accuracy, this requires a good knowledge of the water depth (and in shallow waters an accurate representation of the tides where they are significant) and of the bottom bidirectional reflection function. The latter is unknown for Lunenburg Bay.

[82]   Given the important effects that these two processes have on reflectance (see Figure 13), and thereby on the retrieval of phytoplankton using an absorption-based model, we decided to omit from the inversion the bands where these effects are significant. With increased knowledge of the bay's bottom reflectance and CDOM fluorescence properties, it is likely that we would be able to use these bands. However, it is not clear whether the additional information would lead to estimates of new and important geochemical parameters or to an improved accuracy for those already retrieved. Thus, further efforts are not planned in this direction.

5.4.   Comparison With Published Work

[83]   A principal aim of our study was to verify that we could retrieve a significant portion of the variability of phytoplankton biomass in Lunenburg Bay using Sun-induced fluorescence as a proxy. The retrieval of phytoplankton biomass (always in terms of chlorophyll) from measurements of Sun-induced fluorescence has been attempted by several researchers [e.g., *Cullen et al.*, 1997; *Gower and Borstad*, 1990; *Gower et al.*, 1999; *Kishino et al.*, 1984; *Neville and Gower*, 1977; *Sathyendranath et al.*, 2004; *Yoshikawa and Furuya*, 2004]. The results usually show relatively good retrievals, but most studies have used data sets with ranges of values much larger than in Lunenburg Bay, which in summer has a relatively stable biomass, a factor of 3 to 4 variability. Furthermore, most studies have limited their attempts to a comparison between the fluores-

cence line height (L_{uf} (683)) and chlorophyll concentration. These studies share the limitations inherent to the use of the fluorescence baseline method to extract the fluorescence signal. This method can show biases in Case 1 [*Huot et al.*, 2005] and Case 2 waters with high sediment loads [*Gower et al.*, 1999]. Finally, previous attempts to retrieve chlorophyll concentration from upwelling radiance at the surface do not account for the spectral attenuation of downwelling irradiance and upwelling radiance, nor do they account for effects of irradiance on the quantum yield of fluorescence (e.g., as described by *Morrison* [2003]). Our model, which includes all of these effects, should in theory perform better than these previous attempts. The work by *Chamberlin et al.* [1990] comes closest to our model by taking into account the attenuation of downwelling PAR in their estimation of chlorophyll concentration from FLH; they show retrievals of the chlorophyll with a standard deviation of the error of 47% over a wide range of chlorophyll concentrations. They did not, however, attempt to allow their quantum yield of fluorescence to vary for the accurate retrieval of chlorophyll concentration, nor did they account for spectral effects.

[84]   In our approach, we focus on the retrieval of phytoplankton absorption, which is better correlated to fluorescence measurements than to chlorophyll [*Matorin et al.*, 2004]. This should not be a limitation as, for many applications, phytoplankton absorption is preferable to a measure of chlorophyll concentration [*Perry*, 1994] and provides a more direct link between primary productivity and ocean color [*Lee et al.*, 1996]. This direct relationship forms the basis of the Sun-induced fluorescence method proposed to estimate primary production [*Kiefer et al.*, 1989]. Nevertheless, application of our model to the 2004 data set showed that, for the waters studied, the chlorophyll concentration is also well retrieved using a simple linear relationship between the estimated phytoplankton absorption and measured chlorophyll concentration (Figures 14a and 14b). Accuracy in the retrieval of chlorophyll is easier to compare with other approaches, as our favorable comparison with the OC4V4 algorithm (Figure 14c) shows.

5.5.   Application to Other Environments

[85]   The model was designed for use in Lunenburg Bay using one measurement configuration, but with appropriate modifications, it should be applicable to other locations [see *Huot*, 2004]. If used with the same instrument, two main aspects need consideration: (1) the spectral shape of the absorption components, and (2) the possible need for new look-up tables for waters with a backscattering ratio significantly different from 0.0144. While the first aspect is straightforward and requires only basic knowledge of the waters studied, the creation of new LUTs is much more involved. However, from experience, it is likely to be unnecessary unless one is interested in the accurate retrieval of backscattering using the model, as errors in the absolute value of backscattering do not have large effects on the retrieval of absorption.

6.   Conclusions

[86]   The inverse model of ocean color developed here uses Sun-induced fluorescence in the estimation of phyto-

plankton biomass in coastal waters where the absorption signature of phytoplankton is masked by CDOM absorption. The model also permits the determination of the quantum yield of fluorescence, if the phytoplankton absorption is known or can be estimated (this application is examined by *Huot* [2004], with a previous version of the model). Our goal during its development was to obtain an optical model that is as complete as possible while avoiding spectral regions that cannot be modeled accurately, thus allowing us to reduce the errors associated with the parameterization. This model is coupled to a simple but robust fluorescence model that accounts for first order changes in the quantum yield of fluorescence. This led us to make several improvements with respect to standard ocean color models all of which allowed us to make accurate biomass estimates for our waters (optically shallow with high CDOM concentration). The main improvements are: (1) The utilization of information from both the reflectance and diffuse attenuation coefficient, which allowed a good separation of the effects of backscattering from absorption. (2) Avoiding the utilization of reflectance bands between 400 and 600 nm, thereby avoiding interference from bottom reflection and CDOM fluorescence. (3) The utilization of Sun-induced fluorescence, which provided a clear signal of phytoplankton biomass; the analysis goes well beyond earlier approaches analyzing fluorescence line height. (4) Accounting for the irradiance dependence of the quantum yield of fluorescence, which is necessary to properly convert the observed fluorescence signal to absorption. (5) The utilization of a look-up table dependent on the solar angle, which allowed for estimates of phytoplankton biomass throughout the day and an accurate description of the geometry of our instrument.

[87] Together, these improvements allowed us to obtain estimates of phytoplankton biomass in waters where standard inversion models, empirical relationships based on wavelength ratios, or simple fluorescence models fail. Because the waters studied here are not unlike many coastal waters around the world, this improved formulation could find more widespread application in similarly optically complex waters. Furthermore, our results bode well for the application of remote sensing of Sun-induced fluorescence to coastal waters influenced by CDOM. The model is currently used to retrieve phytoplankton biomass as part of the CMEP (Centre for Marine Environmental Prediction) observation program (http://www.cmep.ca/bay), and can be adapted for other coastal ocean observatories.

Appendix A: Hydrolight Simulations

[88] The Hydrolight simulations were run using absorption and scattering coefficients that are representative of Lunenburg Bay, Nova Scotia. In Lunenburg Bay, absorption is mostly dominated by CDOM, but the results are valid for any location where the backscattering to absorption ratio is in the same range as computed here and where the backscattering ratio is similar.

[89] The Hydrolight simulations are summarized in Table 3. They consist of 2208 model runs (23 spectrally flat nonwater absorption coefficient, 12 spectrally flat nonwater backscattering coefficient, and 8 solar zenith angles) at 66 individual wavelengths. The Fournier-Forand scattering

phase function with a backscattering ratio equal to 0.0144 was used for particulate matter. This backscattering ratio is the mean measured in the surface waters of Lunenburg Bay during the summer of 2002 (Hydroscat backscattering/ac-9 scattering at 640 nm). Absorption by water was from *Pope and Fry* [1997] and scattering was from *Morel* [1973]. The simulated water column was infinitely deep. All runs were done with a clear sky model [*Gregg and Carder*, 1990]. The wind speed, which affects the sea-surface slope distribution function, was set to 3 m s^{-1}. Raman scattering, CDOM fluorescence, and chlorophyll fluorescence were omitted from the runs.

Appendix B: Self-Shading Correction for the Sensor

[90] A method for correcting the measurements from the TSRB instrument for self-shading has been published by *Leathers et al.* [2001]. We will not give details of the method here, but will only describe how we adapted it for our purposes. The *Leathers et al.* [2001] method is based on two look-up tables for the "shading error", one for direct (Sun) and one for diffuse (sky) irradiance. We combine the outputs from these two tables to form the shading error (ε_{shade}, see section 3.5). To use the method, four inputs are necessary under sunny conditions: (i) the zenith angle, (ii) the ratio of direct (Sun) to diffuse (sky) irradiance at each waveband, (iii) the absorption coefficient, and (iv) the scattering coefficient. Under cloudy conditions, only inputs iii and iv are necessary.

[91] In our approach, instead of correcting the measurement of upwelling radiance to reproduce a model without shading, which requires the absorption and scattering coefficients (unknown a priori), we alter the model estimates of reflectance to include the effect of self-shading to reproduce the measurements as affected by absorption and scattering. To do this, the effect of self-shading was accounted for at each step of the iterative optimization procedure as follows.

[92] Inputs i and ii — Firstly, we compute the solar zenith angle, which is then entered into the *Gregg and Carder* [1990] (with standard atmospheric parameters) irradiance model to obtain the ratio of diffuse to direct irradiance (spectrally) and the PAR irradiance above the surface (E_d^{clear}). Secondly, we determine if the conditions are cloudy: if the PAR value measured is less than 80% of the modeled irradiance, the conditions are considered overcast and only the sky radiance look-up table (LUT) is used, otherwise the conditions are considered sunny (clear sky) and both parts of the shading-error LUT are used. If the conditions are sunny, the solar zenith angle and the ratio of diffuse to direct irradiance are entered into the inverse model and used in the shading error LUT.

[93] Inputs iii and iv — At each iteration, the inverse model provides an estimate of the total absorption (input iii) and backscattering coefficients at all wavelengths. The scattering coefficient (input iv) is obtained as $b(\lambda) = b_{bpart}(\lambda)/0.0144 + 2b_{bw}$ where 0.0144 is the mean backscattering ratio obtained in Lunenburg Bay (see Figure 4) and used for the Hydrolight simulations.

[94] With all inputs, the shading LUTs then return the shading correction coefficient, ε_{shade}. This correction coefficient is applied to the modeled reflectance without
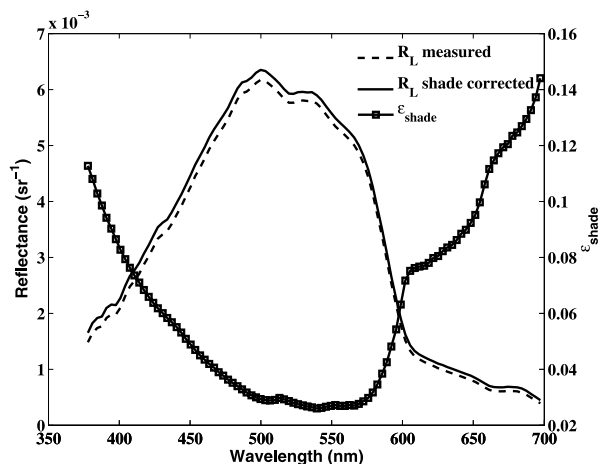
Figure B1. Effect of the shading correction on a reflectance spectrum (same spectrum as used in Figure 12, see Appendix B). The figure shows the measured spectrum (dashed line) and the same spectrum corrected for shading (left axis) as well as the shading error, ε_{shade} (right axis).

self-shading $(\mathbf{R}_{Lb}^{modHL})$ as $\mathbf{R}_{Lb}^{mod}(\lambda|\theta) = (1 - \varepsilon_{shade})\mathbf{R}_{Lb}^{modHL}$ $(\lambda|a_{nw}, b_{bnw}, \theta_{sun})|_{0+}^{0.65}$.

[95] Location specific consideration — For our model, we extended the shading look-up table of *Leathers et al.* [2001] by using a linear extrapolation. Two cases had to be extrapolated, (1) where the absorption was greater than 1 m^{-1}, which occurs occasionally in Lunenburg Bay at short wavebands, and (2) when the b/a is smaller than 1 and the Sun zenith angle is smaller than 30°, which is usually the standard case at the red end of the spectrum in Lunenburg Bay. In the latter case, errors due to the extrapolation are negligible (see look-up tables in *Leathers et al.* [2001]). In the former case they become more important as one departs from 1 m^{-1}, but they are difficult to quantify. The effect of this correction is shown in Figure B1 for one spectrum.

References

Albert, A., and C. D. Mobley (2003), An analytical model for subsurface irradiance and remote sensing reflectance in deep and shallow case-2 waters, *Opt. Express.*, *11*(22), 2873–2890.

Babin, M., et al. (1996a), Nitrogen- and irradiance-dependent variations of the maximum quantum yield of carbon fixation in eutrophic, mesotrophic and oligotrophic marine systems, *Deep Sea Res., Part I*, *43*(8), 1241–1272.

Babin, M., et al. (1996b), Remote sensing of sea surface sun-induced chlorophyll fluorescence: consequences of natural variations in the optical characteristics of phytoplankton and the quantum yield of chlorophyll a fluorescence, *Int. J. Remote. Sens.*, *17*(12), 2417–2448.

Babin, M., et al. (2003), Light scattering properties of marine particles in coastal and open ocean waters as related to the particle mass concentration, *Limnol. Oceanogr.*, *48*(2), 843–859.

Bartlett, J. S., et al. (1998), Raman scattering by pure water and seawater, *Appl. Opt.*, *37*, 3324–3332.

Blough, N. V., and R. Del Vecchio (2002), Chromophoric DOM in the coastal environment, in *Biogeochemistry of Marine Dissolved Organic Matter*, edited by D. A. Hansell and C. A. Carlson, pp. 509–546, Elsevier, New York.

Boss, E., and W. S. Pegau (2001), Relationship of light scattering at an angle in the backward direction to the backscattering coefficient, *Appl. Opt.*, *40*(30), 5503–5507.

Bukata, R. P., et al. (2004), Mitigating the impact of trans-spectral processes on multivariate retrieval of water quality parameters from case 2 waters, *Can. J. Remote Sens.*, *30*(1), 8–16.

Carder, K. L., et al. (1999), Semianalytic Moderate-Resolution Imaging Spectrometer algorithm for chlorophyll a concentration and absorption with bio-optical domains based on nitrate-depletion temperatures, *J. Geophys. Res.*, *104*(C3), 5403–5421.

Chamberlin, W. S., et al. (1990), Evidence for a simple relationship between natural fluorescence, photosynthesis and chlorophyll in the sea, *Deep Sea Res.*, *37*(6), 951–973.

Coble, P. G. (1996), Characterization of marine and terrestrial DOM in seawater using excitation-emission matrix spectroscopy, *Mar. Chem.*, *51*(4), 325–346.

Coleman, J. E., et al. (2000), Utilization of solar-induced chlorophyll a fluorescence as an indicator of phytoplankton biomass in coastal waters, paper presented at Ocean Optics XV, Monaco.

Coleman, T. F., and Y. Li (1994), On the convergence of reflective Newton methods for large-scale nonlinear minimization subject to bounds, *Math. Program.*, *67*(2), 189–224.

Collins, D. J., et al. (1985), The role of reabsorption in the spectral distribution of phytoplankton fluorescence emission, *Deep Sea Res.*, *32*(8), 983–1003.

Cullen, J. J., and M. R. Lewis (1995), Biological processes and optical measurements near the sea-surface: some issues relevant to remote sensing, *J. Geophys. Res.*, *100*(C7), 13,255–13,266.

Cullen, J. J., et al. (1997), The relationship between near-surface chlorophyll and solar-stimulated fluorescence: biological effects, *Ocean Optics XIII, Proc. SPIE*, *2963*, 272–277.

Culver, M. E., and M. J. Perry (1997), Calculation of solar-induced fluorescence in surface and subsurface waters, *J. Geophys. Res.*, *102*(C5), 10,563–10,572.

Demers, S., et al. (1991), Rapid light-induced changes in cell fluorescence and in xanthophyll-cycle pigments of Alexandrium excavatum (Dinophyceae) and Thalassiosira pseudonana (Bacillariophyceae): a photo-protection mechanism, *Mar. Ecol. Prog. Ser.*, *76*, 185–193.

Falkowski, P. G., and Z. Kolber (1995), Variations in chlorophyll fluorescence yields in phytoplankton in the world oceans, *Aust. J. Plant Physiol.*, *22*(2), 341–355.

Fichot, C. G., and W. L. Miller (2002), Towards the remote sensing of CDOM optical properties, paper presented at Ocean Optics XVI, Off. of Nav. Res., Santa Fe, N. M.

Fuchs, E., et al. (2002), The effect of elevated levels of phaeophytin in natural water on variable fluorescence measured from phytoplankton, *J. Plankton Res.*, *24*(11), 1221–1229.

Garver, S. A., and D. A. Siegel (1997), Inherent optical property inversion of ocean color spectra and its biogeochemical interpretation: 1. Time series from the Sargasso Sea, *J. Geophys. Res.*, *102*(C8), 18,607–18,625.

Gordon, H. R. (1974), Spectral variations in the volume scattering function at large angles in natural waters, *J. Opt. Soc. Am.*, *64*(6), 773–775.

Gordon, H. R. (1979), Diffuse reflectance of the ocean: the theory of its augmentation by chlorophyll a fluorescence, *Appl. Opt.*, *21*, 2489–2492.

Gordon, H. R. (1999), Contribution of Raman scattering to water-leaving radiance: a reexamination, *Appl. Opt.*, *38*(15), 3166–3174.

Gordon, H. R. (2002), Inverse methods in hydrologic optics, *Oceanologia*, *44*(1), 9–58.

Gordon, H. R., and W. R. McCluney (1975), Estimation of the depth of sunlight penetration in the sea for remote sensing, *Appl. Opt.*, *14*(2), 413–416.

Gordon, H. R., et al. (1988), A semianalytic radiance model of ocean color, *J. Geophys. Res.*, *93*(D9), 10,909–10,924.

Gower, J. F. R., and G. A. Borstad (1990), Mapping of phytoplankton by solar-stimulated fluorescence using an imaging spectrometer, *Int. J. Remote. Sens.*, *11*(2), 313–320.

Gower, J. F. R., et al. (1999), Interpretation of the 685 nm peak in water-leaving radiance spectra in terms of fluorescence, absorption and scattering, and its observation by MERIS, *Int. J. Remote. Sens.*, *20*(9), 1771–1786.

Gregg, W. W., and K. L. Carder (1990), A simple spectral solar irradiance model for cloudless maritime atmosphere, *Limnol. Oceanogr.*, *35*(8), 1657–1675.

Harrison, A. W., and C. A. Coombes (1988), An opaque cloud cover model of sky short wavelength radiance, *Sol. Energy*, *41*(4), 387–392.

Hawes, S. K. (1992), Quantum fluorescence efficiencies of marine fulvic and humic acids, Master's thesis, 92 pp., Univ. of S. Fla., Tampa.

Hoge, F. E., et al. (2003), Validation of Terra-MODIS phytoplankton chlorophyll fluorescence line height, I. Initial airborne lidar results, *Appl. Opt.*, *42*(15), 2767–2771.

Huot, Y. (2004), Sun-induced fluorescence of phytoplankton in the ocean: linking physiology and remote sensing, Ph.D. thesis, 358 pp., Dalhousie Univ., Halifax.

Huot, Y., et al. (2005), New algorithms for MODIS sun-induced chlorophyll fluorescence and a comparison with present data products, *Limnol. Oceanogr.*, *3*, 108–130.

Johannessen, S. C., et al. (2003), Calculation of UV attenuation and colored dissolved organic matter absorption spectra from measurement of ocean color, *J. Geophys. Res.*, *108*(C9), 3301, doi:10.1029/2000JC000514.

Johnsen, G., et al. (1997), Fluorescence excitation spectra and light utilization in two red tide dinoflagellates, *Limnol. Oceanogr.*, *42*(5), 1166–1177.

Kiefer, D. A. (1973), Fluorescence properties of natural phytoplankton populations, *Mar. Biol.*, *22*, 263–269.

Kiefer, D. A., et al. (1989), Natural fluorescence of chlorophyll a: relationship to photosynthesis and chlorophyll concentration in the western South Pacific gyre, *Limnol. Oceanogr.*, *34*, 868–881.

Kishino, M., et al. (1984), Influence of fluorescence of chlorophyll a on underwater upward irradiance spectrum, *Mer*, *22*, 224–232.

Krause, G. H., and E. Weis (1991), Chlorophyll fluorescence: The basics, *Ann. Rev. Plant Physiol.*, *42*, 313–349.

Leathers, R. A., et al. (2001), Self-shading correction for upwelling sea-surface radiance measurements made with buoyed instruments, *Opt. Express.*, *8*(10), 561–570.

Lee, Z. P., et al. (1996), Estimating primary production at depth from remote sensing, *Appl. Opt.*, *35*(3), 463–474.

Letelier, R., and M. R. Abbott (1996), An analysis of chlorophyll fluorescence algorithms for the Moderate Resolution Imaging Spectrometer (MODIS), *Remote Sens. Environ.*, *58*, 215–223.

Loftus, M. E., and H. H. Seliger (1975), Some limitations of the in vivo fluorescence technique, *Chesapeake Sci.*, *16*, 79–92.

Loisel, H., and A. Morel (1998), Light scattering and chlorophyll concentration in case 1 waters: a reexamination, *Limnol. Oceanogr.*, *43*(5), 847–858.

Loisel, H., and D. Stramski (2000), Estimation of the inherent optical properties of natural waters from the irradiance attenuation coefficient and reflectance in the presence of Raman scattering, *Appl. Opt.*, *39*(18), 3001–3011.

Loisel, H., et al. (2001), Comparison of the ocean inherent optical properties obtained from measurement and inverse modeling, *Appl. Opt.*, *40*(15), 2384–2397.

Lutz, V. A., et al. (1998), Differences between in vivo absorption and fluorescence excitation spectra in natural samples of phytoplankton, *J. Phycol.*, *34*(2), 214–227.

MacIntyre, H. L., and J. J. Cullen (2005), Using cultures to investigate the physiological ecology of microalgae, in *Algal Culturing Techniques*, edited by R. M. Anderson, Elsevier, New York.

Maffione, R. A., and D. R. Dana (1997), Instruments and methods for measuring the backward-scattering coefficient of ocean waters, *Appl. Opt.*, *36*(24), 6057–6067.

Maritorena, S., et al. (2000), Determination of the fluorescence quantum yield by oceanic phytoplankton in their natural habitat, *Appl. Opt.*, *39*(36), 6725–6737.

Maritorena, S., et al. (2002), Optimization of a semianalytical ocean color model for global-scale applications, *Appl. Opt.*, *41*(15), 2705–2714.

Markager, S., and W. F. Vincent (2001), Light absorption by phytoplankton: development of a matching parameter for algal photosynthesis under different spectral regimes, *J. Plankton Res.*, *23*(12), 1373–1384.

Marshall, B. R., and R. C. Smith (1990), Raman scattering and in-water ocean optical properties, *Appl. Opt.*, *29*(1), 71–84.

Matorin, D. N., et al. (2004), Chlorophyll fluorimetry as a method for studying light absorption by photosynthetic pigments in marine algae, *Oceanologia*, *46*(4), 519–531.

Mobley, C. D. (1994), *Light and Water Radiative Transfer in Natural Waters*, 1st ed., 592 pp., Elsevier, New York.

Morel, A. (1973), Diffusion de la lumière par les eaux de mer résultats experimentaux et approche théorique, 161 pp., Univ. de Paris, Villefranche-sur-mer.

Morel, A. (1978), Available, usable, and stored radiant energy in relation to marine photosynthesis, *Deep Sea Res.*, *25*, 673–687.

Morel, A. (1988), Optical modeling of the upper ocean in relation to its biogenous matter content (case 1 waters), *J. Geophys. Res.*, *93*(C9), 10,749–10,768.

Morel, A., and B. Gentili (2004), Radiation transport within oceanic (case 1) water, *J. Geophys. Res.*, *109*, C06008, doi:10.1029/2003JC002259.

Morel, A., and H. Loisel (1998), Apparent optical properties of oceanic water: dependence on the molecular scattering contribution, *Appl. Opt.*, *37*(21), 4765–4776.

Morel, A., and S. Maritorena (2001), Bio-optical properties of oceanic waters: A reappraisal, *J. Geophys. Res.*, *106*(C4), 7163–7180.

Morel, A., et al. (2002), Bidirectional reflectance of oceanic waters: accounting for Raman emission and varying particle scattering phase function, *Appl. Opt.*, *41*(30), 6289–6306.

Morrison, J. R. (2003), In situ determination of the quantum yield of phytoplankton chlorophyll a fluorescence: a simple algorithm, observations, and a model, *Limnol. Oceanogr.*, *48*(2), 618–631.

Mueller, J. L., et al. (2003), Ocean optics protocols for satellite ocean color sensor validation, revision 5, vol. 5, Biogeochemical and bio-optical measurements and data analysis protocols, 43 pp., Natl. Aeronaut. and Space Admin., Greenbelt, Md.

Müller, P., et al. (2001), Non-photochemical quenching: A response to excess light energy, *Plant Physiol.*, *125*, 1558–1566.

Neville, R. A., and J. F. R. Gower (1977), Passive remote sensing of phytoplankton via chlorophyll fluorescence, *J. Geophys. Res.*, *82*, 3487–3493.

Ohi, N., et al. (2002), Diel patterns in light absorption and absorption efficiency factors of *Isochrysis galbana* (Prymnesiophyceae), *J. Phycol.*, *38*, 730–737.

O'Reilly, J. E., et al. (1998), Ocean color chlorophyll algorithm for Sea-WiFS, *J. Geophys. Res.*, *103*(C11), 24,937–24,953.

Ostrowska, M., et al. (1997), An attempt to use measurements of sun-induced chlorophyll fluorescence to estimate chlorophyll a concentration in the Baltic Sea, *Proc. SPIE Int. Soc. Opt. Eng.*, *3222*, 528–537.

Ostrowska, M., et al. (2000a), Variability of the specific fluorescence of chlorophyll in the ocean. Part 1. Theory of classical in situ chlorophyll fluorometry, *Oceanologia*, *42*(2), 203–219.

Ostrowska, M., et al. (2000b), Variability of the specific fluorescence of chlorophyll in the ocean. Part 2. Fluorometric method of chlorophyll a determination, *Oceanologia*, *42*(2), 221–229.

Pegau, W. S., et al. (2003), Inherent optical properties: Instrument, characterization, field measurement and data analysis protocols, 83 pp., Natl. Aeronaut. and Space Admin., Greenbelt, Md.

Perry, M. J. (1994), Measurements of phytoplankton absorption other than per unit of chlorophyll a, in *Ocean Optics*, edited by R. W. Spinrad et al., pp. 107–116, Oxford Univ. Press, New York.

Pope, R. M., and E. S. Fry (1997), Absorption spectrum (380–700 nm) of pure water, II. Integrating cavity measurements, *Appl. Opt.*, *36*(33), 8710–8723.

Pozdnyakov, D., and H. Grassl (2003), *Colour of Inland and Coastal Waters: A Methodology for Its Interpretation*, 1st ed., 170 pp., Praxis, Chichester.

Preisendorfer, R. W. (1976), Hydrologic optics, Natl. Oceanic and Atmos. Admin., Honolulu, Hawaii.

Raateoja, M., et al. (2004), Fast repetition rate fluorometry is not applicable to studies of filamentous cyanobacteria from the Baltic Sea, *Limnol. Oceanogr.*, *49*(4), 1006–1012.

Roesler, C. S. (2003), A novel ocean color inversion model: retrieval of beam attenuation and particle size distribution, *Geophys. Res. Lett.*, *30*(9), 1468, doi:10.1029/2002GL016185.

Roesler, C. S., and M. J. Perry (1995), In situ phytoplankton absorption, fluorescence emission, and particulate backscattering spectra determined from reflectance, *J. Geophys. Res.*, *100*(C7), 13,279–13,294.

Ruban, A. V., et al. (2004), The super-excess energy dissipation in diatom algae: comparative analysis with higher plants, *Photosynth. Res.*, *82*, 165–175.

Sathyendranath, S., and T. Platt (1998), Ocean-color model incorporating transspectral processes, *Appl. Opt.*, *37*(12), 2216–2227.

Sathyendranath, S., et al. (2004), A multispectral remote sensing study of coastal waters off Vancouver Island, *Int. J. Remote. Sens.*, *25*(5), 893–919.

Sciandra, A., et al. (2000), Responses of growth rate, pigment composition and optical properties of Cryptomonas sp. to light and nitrogen stresses, *Mar. Ecol. Prog. Ser.*, *201*, 107–120.

Seritti, A., et al. (1998), DOC, absorption and fluorescence properties of estuarine and coastal waters of the Northern Tyrrhenian Sea, *Chem. Speciation Bioavailability*, *10*(3), 95–106.

Siegel, D. A., et al. (2002), Global distribution and dynamics of colored dissolved and detrital organic materials, *J. Geophys. Res.*, *107*(C12), 3228, doi:10.1029/2001JC000965.

SooHoo, J. B., et al. (1982), In vivo fluorescence excitation and absorption spectra of marine phytoplankton: I. Taxonomic characteristics and responses to photoadaptation, *J. Plankton Res.*, *8*(1), 197–214.

Sosik, H. M., and B. G. Mitchell (1995), Light absorption by phytoplankton, photosynthetic pigments and detritus in the California Current System, *Deep Sea Res., Part I*, *42*(10), 1717–1748.

Stramski, D., and R. A. Reynolds (1993), Diel variations in the optical properties of a marine diatom, *Limnol. Oceanogr.*, *38*, 1347–1364.

Trissl, H.-W. (2003), Modelling the excitation energy capture in thylakoid membranes, in *Photosynthesis in Algae*, edited by A. W. D. Larkum et al., p. 479, Springer, New York.

Vodacek, A., et al. (1994), An experimental model of the solar-stimulated fluorescence of chromophoric dissolved organic matter, *Limnol. Oceanogr.*, *39*(1), 1–11.

Vodacek, A., et al. (1997), Seasonal variation of CDOM and DOC in the Middle Atlantic Bight: Terrestrial inputs and photooxidation, *Limnol. Oceanogr.*, *42*(4), 674–686.

Wang, P., et al. (2005), Uncertainties of inherent optical properties obtained from semianalytical inversions of ocean color, *Appl. Opt.*, *44*(19), 4074–4085.

Werdell, J. P., and S. W. Bailey (2005), An improved bio-optical data set for ocean color algorithm development and satellite data product validation, *Remote Sens. Environ.*, *98*(1), 122–140.

Yentsch, C. S. (1960), The influence of phytoplankton pigments on the colour of sea water, *Deep Sea Res.*, *7*, 1–9.

Yentsch, C. S., and D. W. Menzel (1963), A method for the determination of phytoplankton chlorophyll and phaeophytin by fluorescence, *Deep Sea Res.*, *10*, 221–231.

Yoshikawa, T., and K. Furuya (2004), Long-term monitoring of primary production in coastal waters by an improved natural fluorescence method, *Mar. Ecol. Prog. Ser.*, *273*, 17–30.

Zheng, X., et al. (2002), Variability of the downwelling diffuse attenuation coefficient with consideration of inelastic scattering, *Appl. Opt.*, *41*(30), 6477–6488.

_____

C. A. Brown and Y. Huot, Laboratoire d'Océanographie de Villefranche, F-06230 Villefranche-sur-mer, France. (huot@obs-vlfr.fr)

J. J. Cullen, Department of Oceanography, Dalhousie University, Halifax, NS, Canada B3H 4J1.